Study on Substrate Binding to Human Tryptophan 2,3-Dioxygenase

Eiko Fukumura

Department of Biological Sciences,
Graduate School of Science, Osaka University

Study on Substrate Binding to Human Tryptophan 2,3-Dioxygenase

(ヒト由来トリプトファン2,3-ジオキシゲナーゼへの基質結合に関する研究)

Eiko Fukumura

Department of Biological Sciences,

Graduate School of Science, Osaka University

CONTENTS

ABBREVIATIONS

TDO	tryptophan 2,3-dioxygenase
rhTDO	recombinant human TDO
xTDO	*Xanthomonas campestris* TDO
ralTDO	*Ralstonia metallidurans* TDO
IDO	indoleamine 2,3-dioxygenase
L-Trp	L-tryptophan
IFN-γ	interferon-γ
LPS	lipopolysaccharide
FAD	flabin adenine dinucleotide
FMN	flabin mononucleotide
NAD	nicotineamide adenine dinucleotide
NADH	the reduced form of nicotineamide adenine dinucleotide
NADPH	the reduced form of nicotinamide adenine dinucleotide phosphate
CO	carbon monoxide
4PI	4-phenylimidazole
CN^-	cyanide
cDNA	complementary deoxyribo Nucleic Acid
Amp^r	ampicillin resistant
Cm^r	chloramphenicol resistant
LB medium	Luria-Bertani medium

TB medium	Terrific Broth medium
CCD	Charge Coupled Device
E. coli	*Escherichia coli*
IPTG	isopropyl-β-D(-)-thiogaractopyranoside
CT1 band	charge transfer band
PEG	polyethylene glycol

INTRODUCTION

Prior to 1955, it was thought that the sole role of dioxygen in biological systems was as an electron acceptor in dioxygen-utilizing oxidase or dehydrogenase reactions (*1*). In 1955, two papers reported findings which were in sharp contrast to the classical concept of biological oxidation. By the use of $^{18}O_2$ and $H_2{}^{18}O$ in the reaction catalyzed by mushroom phenolase, Howard S. Mason and his coworkers demonstrated the incorporation of an oxygen atom from molecular oxygen into 3,4-dimethylphenol, producing 4,5-dimethylcatechol (*2,3*) (Fig. i-1). Concurrently, Osamu Hayaishi and his collaborators found that pseudomonad pyrocatechase incorporated two atoms of oxygen from $^{18}O_2$ (but not from $H_2{}^{18}O$) into catechol and produced cis,cis-muconate (*4-6*) (Fig. i-2). These were finding a novel category of the enzymes that directly incorporate oxygen atoms of dioxygen into substrate. Hayaishi designated them as "oxygenases" (*7*). Now, it is established that two types of oxygenases are present in nature: monooxygenases add one oxygen atom, and dioxygenases insert both atoms of molecular oxygen. In addition, it is now known that the oxygenases are widely distributed in nature throughout the plant, animal, and microorganism kingdoms. The oxygenases (*5*) essentially contain metal or flavin as their reaction center (*7*).

TDO was first called "tryptophan pyrrolase" when initially isolated by Kotake and Masayama in 1936, and later "tryptophan 2,3-dioxygenase" by Hayaishi (*8-10*). IDO was isolated initially as a D-Trp-cleaving enzyme from small intestine of rabbit in 1963 by Hayaishi and co-workers (*11,12*). To date, only tryptophan 2,3-dioxygenase (TDO) and indoleamine 2,3-dioxygenase (IDO) have been identified as heme-containing dioxygenases (*13*) (Table. i-1), both of which can catalyze conversion of L-tryptophan

(L-Trp) to *N*-formylkynurenine, by oxidatively cleaving 2,3-bond of the tryptophan pyrrole ring upon incorporation of two oxygen atoms of O_2 (Fig. i-3) (*7,14*). The enzymatic reaction is the first and rate-limiting step in the major metabolic pathway of L-Trp (Fig. i-4).

Although both dioxygenases are cytosolic (soluble) heme proteins and catalyze the same reaction, their physiological role and biochemical properties are distinct (Table i-2) (*1,7,14*). In mammals, IDO is present as a monomeric enzyme, and ubiquitously distributed in all tissues except for the liver (*9,15*). Several possible physiological roles for IDO have been suggested. Most significantly, it is associated with the antiviral and antiproliferative activities of interferon-γ (*1,15-18*). IDO has been shown to be induced *in vivo* in lungs of mice by lipopolysaccharide (LPS) or virus, by IFN-γ (*19–21*). LPS obtained from the cell wall of Gram-negative bacteria, and influenza virus are both known to induce IFN-γ (*22*). Alternatively, it has been shown that local synthesis of the neurotoxin quinolic acid, one of the L-Trp metabolites of the kynurenine pathway, in the central nervous system follows the induction of IDO in macrophage. Thus, IDO is implicated to be of neuropathological significance. The discovery that inhibition of IDO activity reduces the survival of MHC-mismatched fetuses in mice (*23*), and that the risk of fatal allograft rejection correlates with the degree of parental tissue incompatibility (*24*), has led to the hypothesis that IDO activity protects fatal allografts from maternal T-cell-mediated immunity (*25*). Various tumor cell types are known to express IDO (*26*). By promoting antitumor immune responses in combination with cytotoxic chemotherapy, IDO inhibitors may offer a drug-based strategy to more effectively attack systemic cancer (*27-30*).

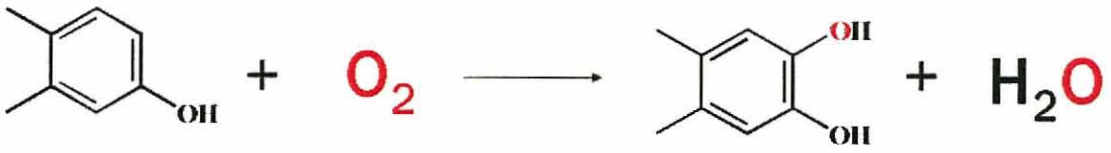

3,4-Dimethyphenol 4,5-Dimethylcatechol

Fig. i-1. The reaction catalyzed by phenolase.

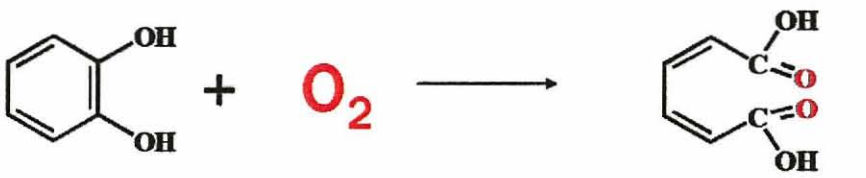

Catechol cis, cis-Muconate

Fig. i-2. The reaction catalyzed by pyrocatechase (catechol 1,2-dioxygenase).

Table. i-1. Classification of oxygenases based on their reaction.

Type	Monooxygenase	Dioxygenase
Reaction	$RH + O_2 + 2e^- + 2H^+ \rightarrow ROH + H_2O$	$R + O_2 \rightarrow R(O)_2$
Cofactor and examples	heme: cytochrome P450 heme oxygenase non-heme iron: methane monooxygenase FAD: arginine 2-monooxygenase FMN: bacterial luciferase cupper: dopamine β-monooxygenase	heme: Tryptophan 2,3-dioxygenase Indoleamine 2,3-dioxygenase non-heme iron: catechol 1,2-dioxygenase protocatechuate 3,4-dioxygenase

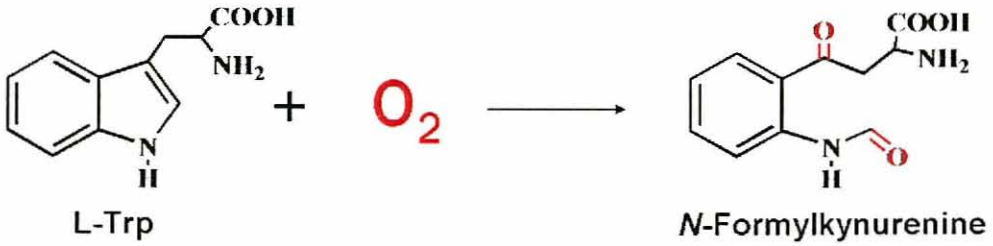

L-Trp *N*-Formylkynurenine

Fig. i-3. The reaction catalyzed by IDO and TDO.

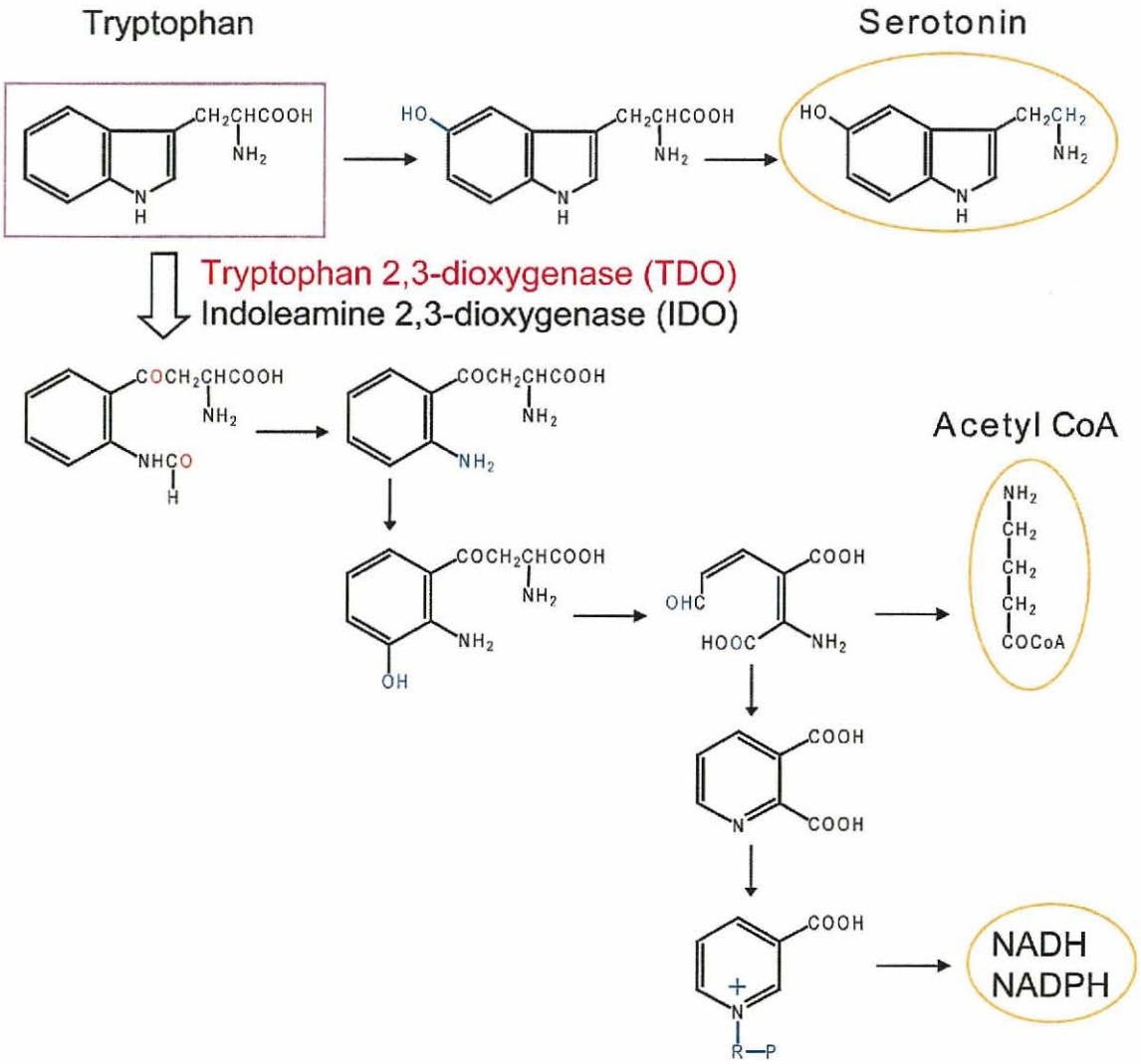

Fig. i-4. Tryptophan metabolism.

Table. i-2. Similalities and distinctions between IDO and TDO.

	IDO	TDO
molecular weight	45,000	122,000 (*Pseudomonas*) 191,000 (mammalian liver)
subunits	1	4 (α_4)
prosthetic group	heme *b* (protoheme IX)	heme *b* (protoheme IX)
substrates	L-Trp, D-Trp 5-hydroxy-L-Trp 5-hydroxy-D-Trp tryptamine serotonin	L-Trp 5-fluoro-L-Trp 6-fluoro-L-Trp
distributions	mammalian ubiquitous (except liver)	mammalian ubiquitous (mainly liver) amphibian fish insect bacteria
inducers	interferon-γ	glucocorticoids

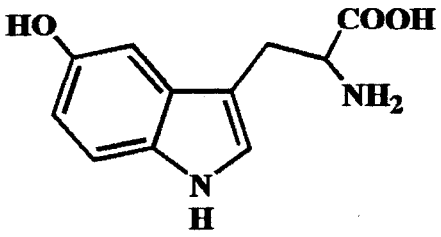

5-hydroxy-tryptophan

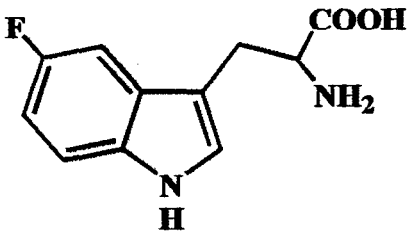

5-fluoro-tryptophan

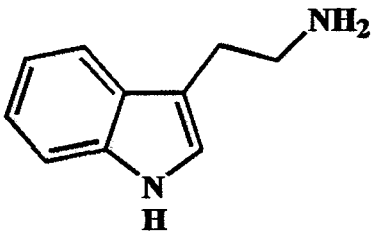

tryptamine

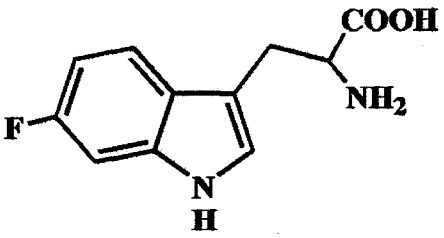

6-fluoro-tryptophan

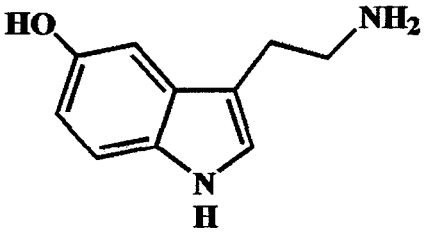

serotonin

Fig. i-5. Indole compounds other than Trp as substrates for IDO or TDO.

In contrast, TDO, which shares no sequence homology with IDO, is widely distributed across species, ranging from bacteria to mammals, as a homo-tetrameric enzyme (*1,31,32*). In mammals, TDO is mainly present in the liver, but, recently, the enzyme was detected in the brain, epidermis, spermatozoa, placenta, and so on (*33-36*). Unlike IDO, which exhibits broad substrate specificity for the indoleamines, the activity of TDO is specific for L-Trp (Table i-2, Fig. i-5) (*1,12,37*). It has been indicated that glucocorticoids administration increases the rate of enzyme synthesis, whereas L-Trp administration decreases the rate of degradation of the enzyme (*32,38-44*). Thus, TDO is induced by glucocorticoids and is also regulated by the availability of the physiological substrate, L-Trp.

It has been shown that TDO exists as tetramer and behaves as an allosteric enzyme. TDO isolated from *Xanthomonas pruni* shows sigmoidal kinetics and its activity is inhibited by intermediates of the NAD biosynthetic pathway (*45*). Its cooperativity is enhanced by anthranilic acid and is diminished by α-methyl Trp (Fig. i-6). Early studies of rat liver TDO also showed that NADPH and 3-hydroxy anthranilate, which are downstream metabolites of L-Trp, are negative modulators of TDO activity (Fig. i-6) (*46,47*). These data indicate that TDO might be regulated by feedback control and that the enzyme has multiple binding sites for L-Trp and its metabolites.

In sharp contrast to heme-containing monooxygenases (such as cytochrome P450 and heme oxygenase) and nonheme dioxygenases (such as catechol 1,2-dioxygenases and protocatechuate 3,4-dioxygenase), chemistry for the IDO and TDO reaction remains elusive, even thought they were discovered more than 40 years ago. It is mainly due to the lack of crystallographic study and observation of the proposed intermediates, as well as due to the fact that no similar reaction is observed in the other heme-containing oxygenases.

Very recently, however, three groups independently obtained the crystal structures of IDO and TDO, and advanced our understanding of molecular mechanism of heme-containing dioxygenase. Structural analysis of human IDO (hIDO) in complex with the ligand inhibitor 4-phenylimidazole (4PI) or cyanide (CN^-) combined with site-directed mutagenesis studies showed that polar amino acid residues in the active site do not play an important role in the enzymematic reaction (*48*). The crystal structures of *Ralstonia metallidurans* TDO (ralTDO) and *Xanthomonas campestris* TDO (xTDO) has been recently resolved by Ealick *et al.* (*49*) and Tong *et al. (31)*, independently. It was surprising that the overall fold in the tertiary structure of IDO and a monomeric subunit of TDO look very similar, although their amino acid sequences share little homology (<15%). Structures of xTDO were determined as a ligand-free form and ferrous form in a binary complex with the substrate L-Trp, in which the carboxylate and ammonium moieties of L-Trp make are recognized by electrostatic and H-bonding interactions with some residues of the enzyme and the heme propionate group, defining the L-stereospecificity. Although the structure analysis of ralTDO revealed important active site residues, it did not provide any information regarding the substrate binding, due to lack of the substrate in the crystal structure.

The crystallographic analysis of recombinant xTDO revealed two different L-Trp-binding sites and extensive interaction between the subunits of the tetramer (Fig. i-7). Although the TDO structure suggests that it has a cooperative mechanism, there is no direct evidence for homotropic cooperative binding of L-Trp to xTDO, as the measurement of the dioxygenase activity reveals Michaelis-Menten-type kinetics. Moreover, the residues in the L-Trp-binding sites which were observed at the tetramer interface of xTDO are not conserved among the species. Thus, the structural mechanism

of the regulation by substrate (homotropic allosteric modulation) and by metabolites (heterotropic allosteric modulation) is not well understood.

It has been reported that the affinity of TDO for its ligands, carbon monoxide (CO) and cyanide (CN^-), is increased in the presence of L-Trp (*50-53*). It is estimated that the binding of L-Trp to TDO causes increasing the affinity for its ligands by substrate-induced conformational change and the alteration in the electronic state of heme iron. Substrate binding usually causes a conformational change in the enzyme. The conformational change is associated with activation enzyme including the prosthetic group. The reaction of oxygenases certainly causes either or both oxygen activation by heme iron and substrate activation. To elucidate the substrate recognition and catalytic mechanism of TDO, it is necessary to reveal how the conformation of the heme and active site residues are affected by substrate binding and how the active-site structure is related to the activation of the substrate or dioxygen for the dioxygenase reaction.

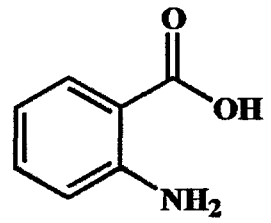

anthranilic acid

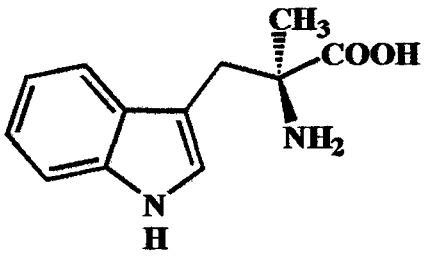

α-methyl tryptophan

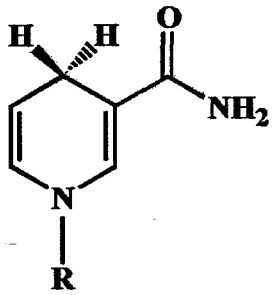

NADPH

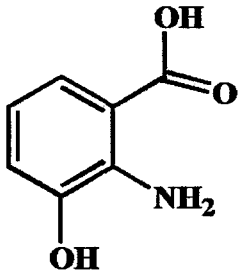

3-hydroxy anthranilate

Fig. i-6. The reported effector compounds of TDO.

R: adenine dinucleotide phosphate.

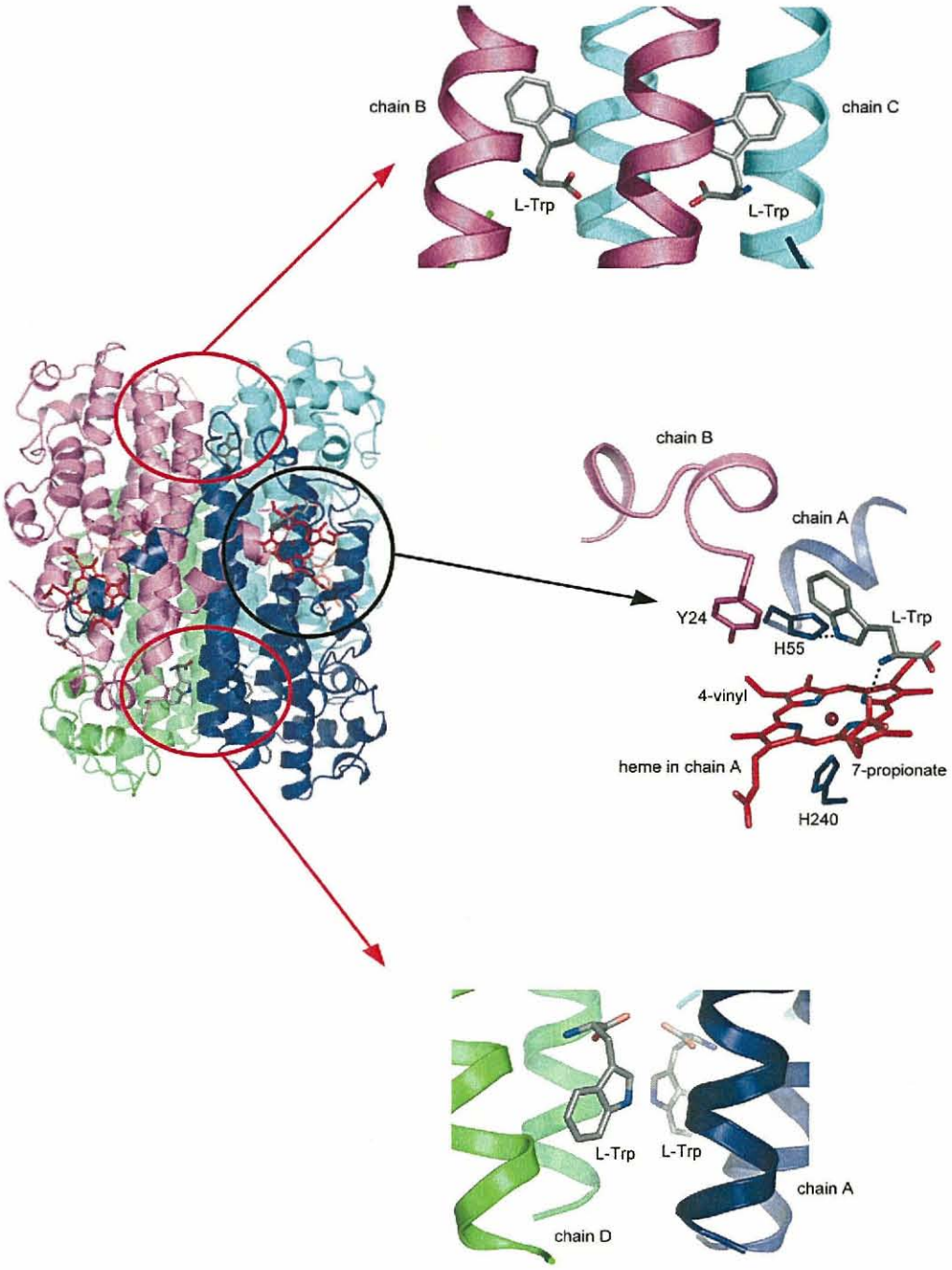

Fig. i-7. Crystal structure of *Xanthomonas campestris* TDO (xTDO).

Black circle indicates the active site of xTDO. Red circles indicate the L-Trp-binding sites which were observed at the tetramer interface of xTDO.

In this thesis, spectroscopic and crystallographic analyses of recombinant human TDO (rhTDO) are described. In chapter I, the analysis of conformational changes in the heme of recombinant human TDO (rhTDO) using resonance Raman and optical absorption spectroscopies are described. The technique of resonance Raman spectroscopy provides structural information, through the vibrational characteristics of the heme in active center. The results demonstrate that rhTDO cooperatively binds substrate, L-Trp. In addition, the mutation analysis revealed essential residues for the cooperative L-Trp binding, which provides insight into the mechanism of homotropic allosteric regulation.

Although most of amino acid residues in the active site of TDO appears to be conserved among bacterial and mammal, amino acid sequences of mammalian TDO has 100 residues larger than bacterial TDO. Therefore, function of residues unique in mammalian TDO still remains understood. In addition, roles of the conserved distal His residue is still controversial. Although H55 of xTDO is involved in substrate interaction (Fig. i-6), site-directed mutagenesis study showed that H55 of xTDO do not play an important role in the enzymatic reaction. Thus, X-ray crystallographic analysis is necessary to gain direct insight into the substrate recognition and the catalysis by hTDO. In chapter II, the crystallization and preliminary crystallographic analysis of rhTDO are described.

CHAPTER I

Cooperative Binding of L-Trp to Human Tryptophan 2,3-Dioxygenase : Resonance Raman Spectroscopic Analysis

SUMMARY

Tryptophan 2,3-dioxygenase (TDO) is a tetrameric enzyme that catalyzes the oxidative cleavage of L-tryptophan (L-Trp) to *N*-formylkynurenine by the addition of O_2 across the 2,3-bond of the indole ring. This reaction is the first and rate-limiting step in the kynurenine pathway in mammals. In the present study, we measured the conformational changes in the heme pocket of recombinant human TDO (rhTDO) in ferric form that are induced by L-Trp binding using both resonance Raman and optical absorption spectroscopies. The deconvolution analysis of the heme Raman bands at various concentrations of L-Trp revealed that the wild-type enzyme exhibits homotropic cooperativity in L-Trp binding, which was confirmed by a change in the optical absorption spectra. Mutation analysis showed that the Y42F mutant abolished the cooperative binding, and that the H76A mutant considerably reduced the catalytic activity. These data and the inter-subunit contacts reported in the bacterial TDO structure suggest that the Y42 of rhTDO is responsible for the cooperative binding of L-Trp by participating in the active site of the adjacent subunit.

MATERIALS AND METHODS

Construction of Expression Plasmid

Human tryptophan 2,3-dioxygenase (hTDO) cDNA (Image clone 4071714) in the pDNR-LIB vector was purchased from American Type Culture Collection. First, we constructed, expressed, and purified full-length hTDO. N-terminal sequence analysis of the purified full-length hTDO revealed that it was truncated at the N-terminal end, with loss of up to 15 amino acid residues. Thus, we constructed rhTDO, and deleted the 15 residues at the N-terminus. The hTDO cDNA was amplified by PCR using a forward primer (5'-GGG CATATG AAAAAACTCCCCGTAGAAGG-3'), which encodes an *Nde*I site (underlined), followed by the coding sequence starting at Met connected to K16, and a reverse primer (5'-GGGGATCCTTAATCTGATTCATCACTG CTGAAGTAGG-3'), which contains the coding sequence up to the termination codon, followed by an *BamHI* site (underlined). This amplified fragment was directly ligated to *Nde*I/*Bam*HI-digested pET15b with a hexa-histidine tag and a thrombin site fused to the N-terminus of hTDO-ΔN15, to produce pET15b hTDO-ΔN15. Two other mutants (H76A, Y42F) were prepared using the QuikChange site-directed mutagenesis kit (Stratagene) with pET15b hTDO-ΔN15 as a template. Plasmids containing pET15b hTDO-ΔN15 and the mutants were used to transform *E. coli* DH5α cells. All constructs were verified by DNA sequencing.

Expression of Recombinant Human TDO

E.coli Rosetta (DE3) pLysS cells were transformed using the plasmid construct. Single colonies on LB-agar plates containing ampicillin (100 μg/ml) and chloramphenicol (70 μg/ml) were selected, and the cells were grown overnight at 37°C

in 2 ml of LB medium containing 100 μg/ml of ampicillin and 70 μg/ml chloramphenicol. The overnight culture (0.5 ml of culture) was used to inoculate 2 L of TB medium (yeast extract, 24.0 g/L; polypeptone, 12.0 g/L; glycerol, 0.4% w/v; KH_2PO_4, 2.31 g/L; and, K_2HPO_4, 12.5 g/L) supplemented with 100 μg/ml ampicillin, 70 μg/ml chloramphenicol, 0.5 mM δ-aminolevulinic acid and 0.2 mM Fe_2SO_4. The cultures were grown in TB medium until OD_{600} = 1.1-1.3, and protein expression was induced with 0.5 mM IPTG. The cells were then cultured for ~20 h at 30°C, followed by centrifugation at 10,000 × *g* for 10 min at 4°C. The cell pellets were stored at -80°C until they were used for protein purification.

Purification of Recombinant Human TDO

Frozen cell pellets were resuspended in 120 mL of lysis buffer (50 mM potassium phosphate (pH 8.0), i.e., buffer A) containing EDTA-free complete protease inhibitor cocktail tablets (Roche), lysozyme (0.1 mg/ml), and DNaseI (0.01 mg/ml), followed by stirring for 1 h. Cells were lysed by sonication, and the cell debris was removed by ultracentrifugation at 185,000 × *g* for 30 min at 4°C. The resulting supernatant was loaded onto a Ni-NTA agarose (Qiagen) column that had been equilibrated with lysis buffer supplemented with 300 mM NaCl (buffer B). The column was washed with the same buffer containing 50 mM imidazole (buffer C), and His-tagged proteins were eluted from the column using the same buffer containing 300 mM imidazole (buffer D). The His tags were cleaved by direct addition of biotinylated thrombin (Novagen) to the elutant, which was then dialyzed against buffer B overnight at 4°C. The thrombin-treated protein solution was then loaded onto a Ni-NTA column that had been equilibrated with buffer B. After an additional wash with buffer A, cleaved rhTDO was separated from the uncleaved His-tagged proteins by elution with buffer C. The eluted

protein was concentrated and further purified using a Superdex-200 size-exclusion column with buffer A containing 200 mM NaCl (buffer E). The fractions that contained molecules similar in size to tetrameric hTDO were pooled, and concentrated using Amicon Ultra-15 centrifugal filter devices (Millipore) containing a cellulose filter with a 50-kDa cutoff. After concentration of the fractions, the solution was filtered with a 0.22-μm disposable filter. The concentration of the purified recombinant hTDO was estimated using the pyridine hemochrome assay (*54,55*). The heme *b* extinction coefficient used in this study was $\varepsilon_{557} - \varepsilon_{541} = 20.7\ mM^{-1}cm^{-1}$ (*56*). The concentrated sample was flash-frozen in liquid nitrogen, and stored at -80°C until further use.

Enzyme Assay

The activity of ferric hTDO was measured in buffer E at 37°C under normal atmospheric conditions. The rate of *N*-formylkynurenine formation was monitored at 321 nm ($\varepsilon = 3{,}750\ M^{-1}cm^{-1}$) (*57*). The reaction was initiated by the addition of ferric rhTDO, and after the small lag phase, the linear velocity was measured. The enzyme concentration was 0.5 μM in a final volume of 2.0 ml. During the measurements, the reaction medium was gently stirred in a cuvette with a 1-cm light path. The kinetic data were fitted to the Michaelis-Menten equation using IGOR Pro 5.05 software (WaveMetrics, Inc.).

Raman Spectroscopy

The purified rhTDO, buffer E, and buffer E containing 5 mM L-Trp were each dispensed into small glass vials. Each vial was sealed with a rubber stopper and an open-top screw cap. All vials were deoxygenated by repeated evacuation and flushing with N_2 gas. To establish strictly anaerobic conditions, the de-aerated vials were passed

into an anaerobic glove box (O_2 < 5 ppm), where they were kept for at least 12 h at 4°C. Samples with an enzyme concentration of 300 μM (75 μM of tetramer) and various concentrations of L-Trp were prepared in the glove box using these stock solutions. For measurements of the Raman spectra, the sample solutions were put into a cylindrical quartz cell with a small magnetic stir bar, and the cell was secured with a rubber septum.

Raman scattering was excited at 413.1 nm using a Kr ion laser (Spectra Physics). The Raman scattered light passed through a depolarizer and the entrance slit of a 1.0-m monochromator equipped with a 1,200 groove/mm ruled grating blazed at 500 nm (MC-100DG, Ritsu Ohyo Kogaku Co., LTD). The detector was a 1,100 × 330 pixel, back-illuminated, liquid nitrogen-cooled charge-coupled device detector (LN/CCD-1100PB, Roper Scientific). The entrance slit-width of the monochromator was set at 250 μm. The cylindrical cell was spun at 1,200 rpm to minimize local heating. A holographic notch filter was used to eliminate Rayleigh scattering. The frequency calibration of the spectrometer was performed with indene as the standard. The laser power was maintained at 300 μW for all measurements. The acquisition time was 30 min for all of the spectra obtained. Winspec/32 software (Roper Scientific) was used for data acquisition. Spectral analysis was performed using IGOR Pro5.05 (WaveMetrics, Inc.). After subtracting the best-fit linear baseline from the data, the Gaussian function was used in the fitting procedure for multiple overlapping peaks. Gaussian fitting and peak area calculations were carried out using the Igor Pro multi-peak fitting package.

UV-visible Absorption Spectroscopy

The protein solutions used for the measurement of absorption spectra were prepared by the same protocol as in Raman experiments. The protein and L-Trp solutions were

mixed into the quartz cell with a screw cap and the desired concentration in an anaerobic glove box. The UV-visible region of absorption spectra was measured with an enzyme concentration of 4 μM in the absence and presence of 5 mM L-Trp at 20°C under a N_2 atmosphere. The absorption change in the visible region (530-700 nm) by L-Trp titration was measured with 240 μM of enzyme by the addition of a small volume of 50 mM L-Trp to the enzyme in the glove box. All experiments of optical absorption spectra were performed using a Hitachi U-3000 spectrophotometer equipped with a thermoelectric cell holder and an SPR-10 temperature controller. The temperature of the spectrometer was controlled at 20°C using a water bath (Lauda thermostat RM6).

RESULTS

N-terminal Truncation of rhTDO

First, the plasmids encoding full-length rhTDO with a His tag at N- or C-terminus were constructed. The C-terminal His-tagged rhTDO could express very small amount. The N-terminal His-tagged rhTDO in full-length form was express at higher level but difficult to be purified because of severe aggregation and instability. SDS-PAGE of purified N-terminal His-tagged full-length rhTDO showed the presence of three distinct bands between 37 and 50 kDa (Fig. 1). The N-terminal amino acid sequence of these components analyzed by automated Edman degradation revealed that there are four species. Three of them appeared to be cleaved by proteases. The cleavage sites are between F6 and L7, Y13 and T14, or F15 and K16. On the other hand, the construct of rhTDO with deletion of the N-terminal 15 amino residues (rhTDO-ΔN15) gave a single band on SDS-PAGE. The N-terminal sequence analysis showed the band includes only one sequence. The truncated form of the enzyme (rhTDO-ΔN15) was comparatively stable and used for all biochemical and spectroscopic experiments.

Design of Mutation

As shown in Fig. 2, crystallographic analysis of xTDO revealed that the interaction of xTDO with L-Trp involves the H-bond between H55 and the N1 atom of L-Trp. This observation suggests that the role of H55 in the catalytic activity of the enzyme might be the abstraction of a proton due to the basic nature of the amino acid (*31*). However, the residual activity (15% in k_{cat}) of the H55A mutant suggests another possibility for the roles of this residue in the catalytic reaction, which is still a matter of debate (*58*).

On the other hand, the residue of the adjacent subunit in the xTDO structure, Y24, participates in the formation of the active site and interacts with the 4-vinyl group and the indole ring of L-Trp by hydrophobic interaction. The key residues in the catalytic site of xTDO, H55 and Y24, are conserved in hTDO as H76 and Y42, respectively (Fig. 3). We prepared two mutants of rhTDO (H76A and Y42F) and characterized their enzymatic and spectroscopic properties.

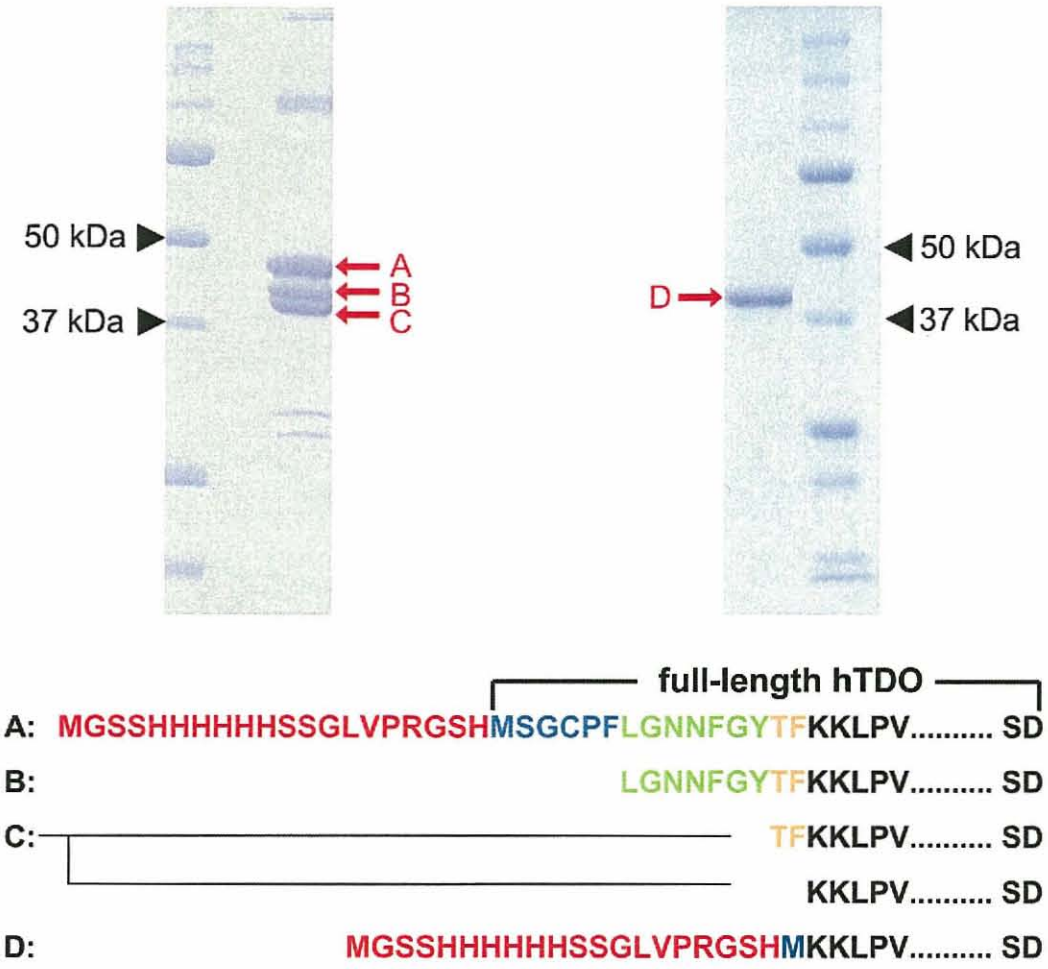

Fig. 1. SDS-PAGE of full-length and the N-terminal truncated rhTDO.
The lane on the left-hand side indicated by arrows A-C is purified full-length rhTDO. The lane on the right-hand side indicated by arrow D is purified rhTDO-ΔN15. The results of N-terminal sequence analysis on A-D bands showed under the SDS-PAGE.

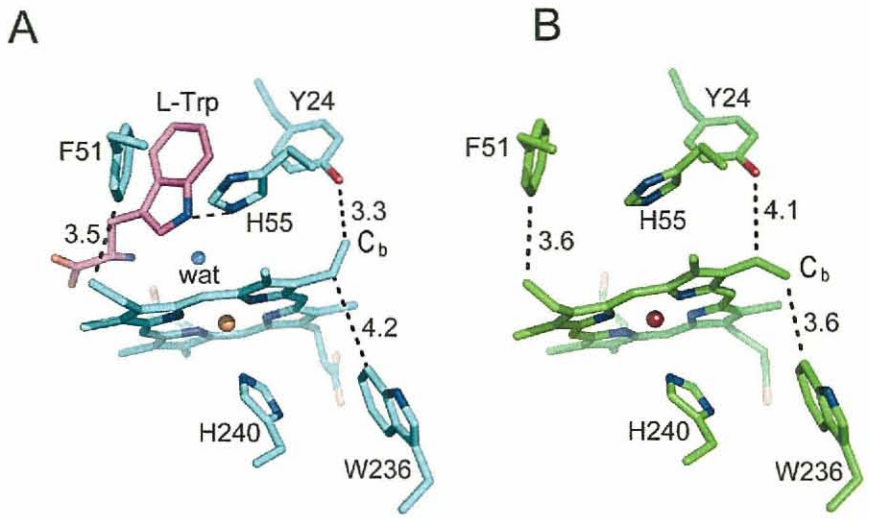

Fig. 2. Active site of *Xanthomonas campestris* TDO.

(A) substrate-bound and (B) substrate-free forms are depicted as ball-and-stick models, with the carbon atoms shown in cyan and green, respectively. The carbon atoms of the substrate, L-Trp, are shown in magenta. Oxygen, nitrogen, and iron atoms are shown in red, blue and brown, respectively. The conformation of the 4-vinyl group of the heme differs significantly between the substrate-bound and -free forms. The C_b atom interacts with Y24 in the L-Trp bound form, but with W236 in the free form. Figures were prepared with the PyMOL program (*59*) using PDB codes 2NW7 and 2NW8.

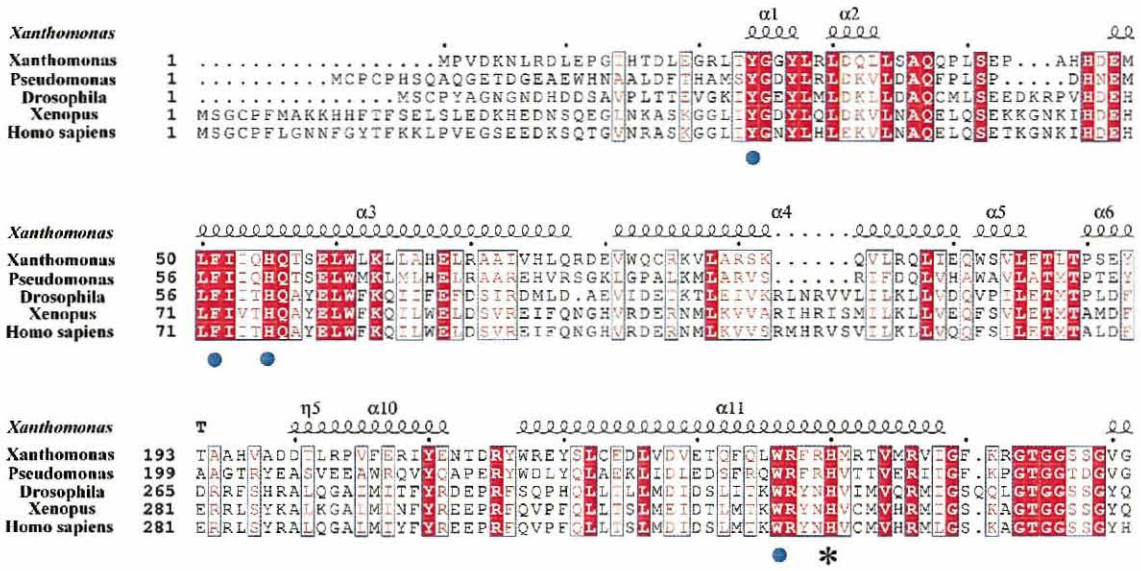

Fig. 3. Partial sequence alignment between the *Xanthomonas campestris* TDO subunit and that of several organisms.

Sequences displayed are those from: Xanthomonas (*Xanthomonas campestris pv. campestris*), Pseudomonas (*Pseudomonas aeruginosa* PA7), Dorosophila (*Dorosophila melanogaster*), Xenopus (*Xenopus leavis*), Homo sapiens (*Homo sapiens*). The completely conserved proximal His residues are marked with an asterisk. Residues in the heme pocket of xTDO, Y24, F51, H55 and W236 are identical to Y42, F72, H76 and W324 of hTDO, respectively. These residues are indicated by the filled circles. The figure was produced using ESPript 2.2 (*60*) and CLUSTAL W (*61*).

Activity of Ferric hTDO

The enzymatic activities of wild-type rhTDO, and of the Y42F and H76A mutants in the ferric state, were measured using various concentrations of the substrate, L-Trp. Previous studies have demonstrated that the ferric enzyme has the capability to degrade L-Trp (*62*). The rate of the product formation under open-air conditions (~400 μM) was plotted against the applied L-Trp concentration, as shown in Fig. 4. The plot was fitted with the Michaelis-Menten equation, providing the apparent kinetic parameters [$K_{m(app)}$, $k_{cat(app)}$], that is compiled in Table 1.

The enzymatic activity of wild-type rhTDO in the ferric state was measured in presence of 5 mM L-Trp, using various concentrations of the oxygen. However, our attempt to obtain the kinetic parameters was unsuccessful, because the data exhibits a biphasic behavior and cannot be fitted with the Michaelis-Menten equation (Fig. 5). Although the simulation of the enzyme model by Martin-Neito *et al.* has suggested that two different forms of enzyme or the enzyme with two cooperative, equivalent sites could exhibit biphasic kinetics (*63*), additional data including pre-steady state kinetics would be necessary for elucidating the oxygen binding property. The data of Fig. 5 show that the activity reaches to the saturation at oxygen concentration of ~60 μM, while the activity data of Fig. 4 was obtained under open air (>400 μM). Thus, the true K_m or k_{cat} values for L-Trp binding appear to be comparable with their apparent values. The obtained $K_{m(app)}$ of wild type (82.5 μM) is comparable to the L-Trp concentration found in the liver of rats with normal diets (40-90 μmol/kg liver) (*64*). As shown by the values of $k_{cat(app)}/K_{m(app)}$, the enzymatic activity of rhTDO was reduced to 3% and 0.1% in the Y42F and H76A mutants, respectively. This result suggests that both residues make significant contributions to the enzymatic reaction of rhTDO. In the case of the Y42F mutation, the change in $K_{m(app)}$ is mainly responsible for the loss of enzymatic

activity, while both $K_{m(app)}$ and $k_{cat(app)}$ are significantly reduced in the H76A mutation.

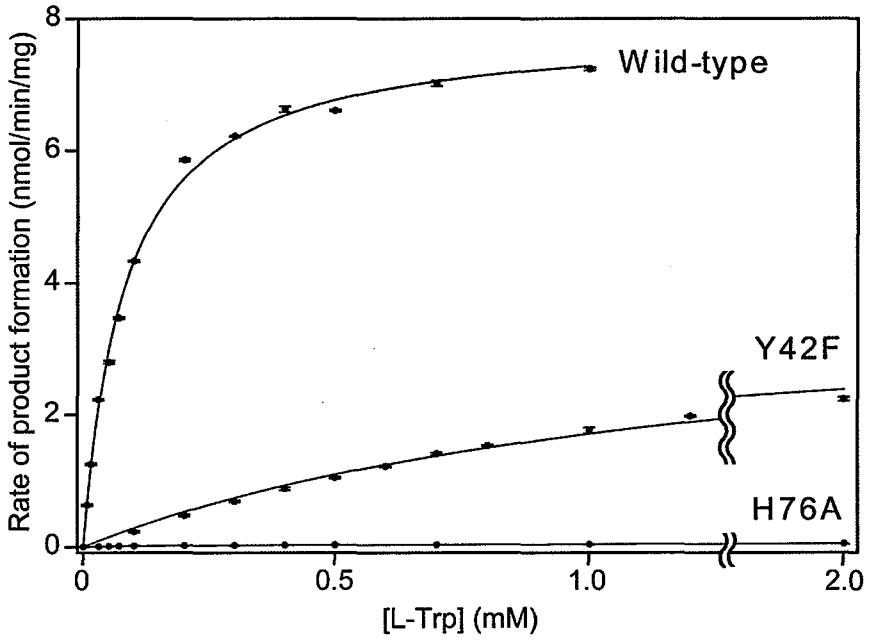

Fig. 4. Rate of product formation *versus* substrate concentration.
Initial reaction rate of wild-type rhTDO, and of the H76A and Y42F mutants plotted as a function of L-Trp. Each value is the mean of three replicates with error bars representing the standard deviation of each sampling point. Kinetic parameters were estimated by fitting the data to the standard Michaelis-Menten equation and are shown in Table 1. The reaction experiments were performed with an enzyme concentration of 0.5 μM, at 37°C, in 50 mM potassium phosphate buffer, pH 8.0.

Table 1: Apparent kinetic parameters for oxidation of L-Trp by ferric rhTDO and its mutants.

	rhTDO (pH 7.0)[a]	rhTDO (pH 8.0)	H76A (pH 8.0)	Y42F (pH 8.0)
$K_{m(app)}$ (μM)	180	82.5 ± 3.8	488 ± 51	1,290 ± 140
$k_{cat(app)}$ (s^{-1})	0.6	6.12 ± 0.02	0.04 ± 0.00	3.04 ± 0.04
$k_{cat(app)}/K_{m(app)}$	3×10^{-3}	7.42×10^{-2}	9×10^{-5}	2.36×10^{-3}

[a] Batabyal, D. and Yeh, S. R. published results.

Experiments were performed with an enzyme concentration of 0.5 μM, at 37°C, in 50 mM potassium phosphate buffer, pH 8.0.

It should be noted that these rates were determined under normal atmospheric conditions.

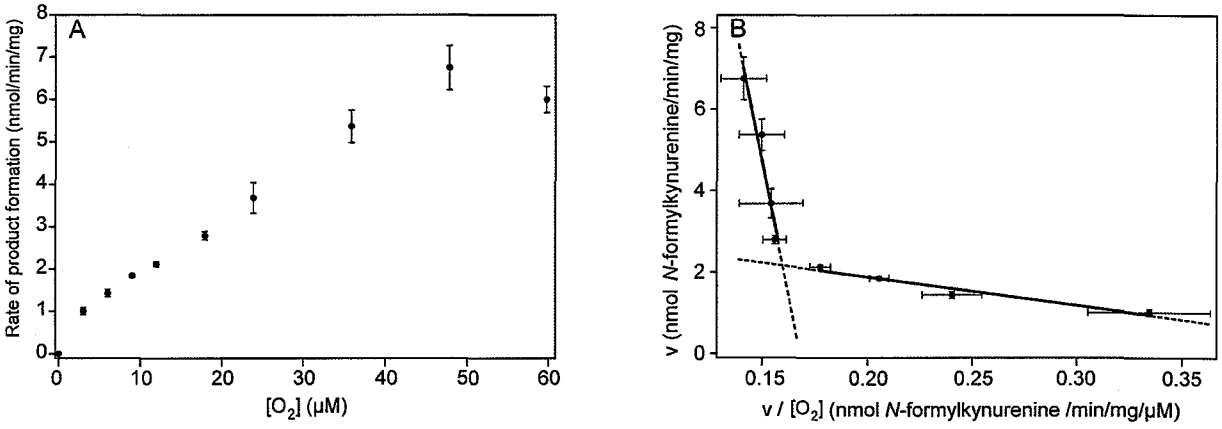

Fig. 5. Reaction of wild-type ferric rhTDO with O_2 in the presence of 5 mM L-Trp.

(A) The product formation rates are plotted as a function of O_2 concentration. (B) Eadie-Hofstee plot of the effect of oxygen concentration on rhTDO activity. Each plotted value for the wild-type is the mean of triplicate measurements and the error bars indicate the standard deviation.

Absorption Spectra of Wild-Type rhTDO

The absorption maxima in the optical absorption spectra of the wild-type rhTDO in ferric form, measured at pH 8.0, are shown in Fig. 6 A. A Soret maximum was observed at 405 nm, α/β bands were observed at 585/504 nm, and a charge transfer band (CT1) was observed at 632 nm. These characteristics are consistent with the spectral features of heme proteins in the ferric, high-spin state (*56*). Upon addition of the substrate, L-Trp, the spectrum was significantly altered: the Soret maximum was red-shifted from 405 to 408 nm, new α/β bands appeared at 574 and 540 nm, and CT1 band was reduced, but did not completely disappear (Fig. 7 A). The spectral change was attributed to a mixture of the low- and high-spin states in heme iron after binding of the L-Trp to rhTDO, which is consistent with the results of Raman experiments.

The sigmoidal kinetics of L-Trp binding observed in Raman spectral change is supported by the absorption spectral change, as shown in Fig. 7 B. The Hill coefficients estimated from the intensity of 632 and 574 nm are 3.3 and 3.2, respectively. These values are slightly larger than those estimated from Raman spectra, mostly because the data point was extended to a higher concentration of L-Trp in the measurement of the absorption spectra.

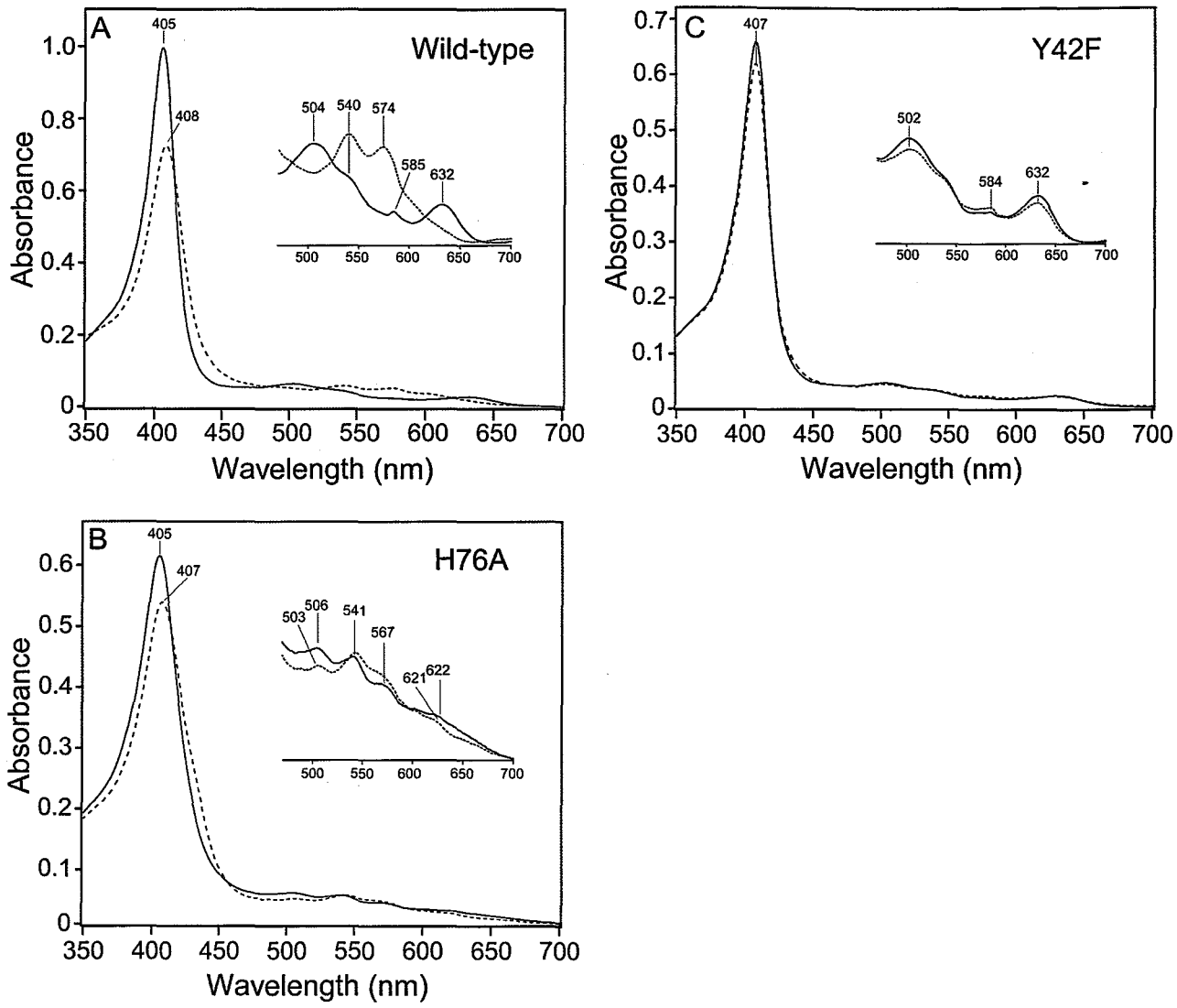

Fig. 6. Absorption spectra of rhTDO and its mutants.

(A) Spectra of wild-type rhTDO, (B) H76A mutant and (C) Y42 mutant in the absence (solid line) and presence (dotted line) of 5 mM L-Trp. Solutions were prepared with 4 μM enzyme in 50 mM potassium phosphate (pH 8.0) under anaerobic conditions. The inset is the expanded view of the visible bands.

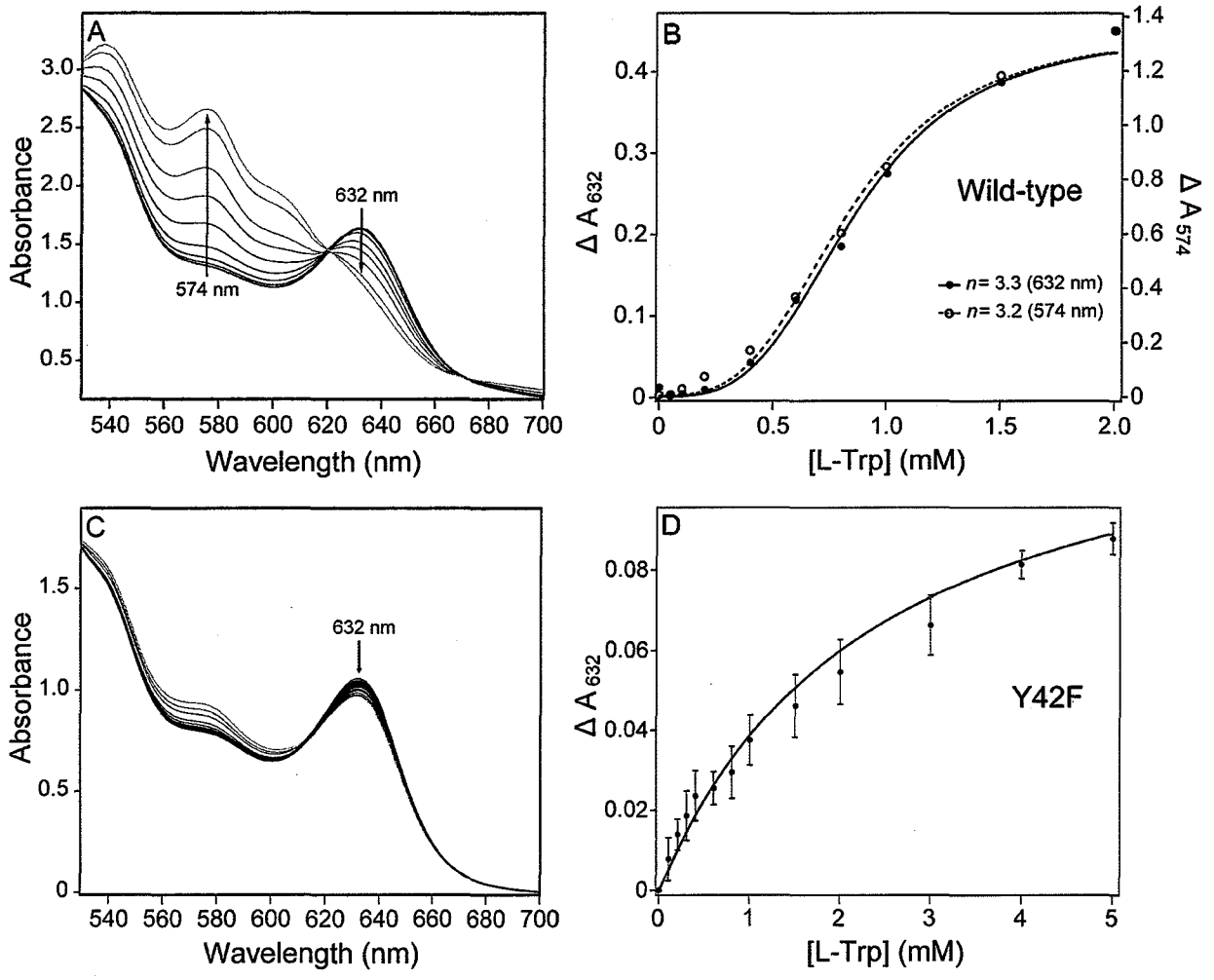

Fig. 7. Change of absorption spectra by the addition of L-Trp.

(A) The visible region of absorption spectra of wild-type enzyme upon successive additions of L-Trp. (B) The intensity of the CT1 band at 632 nm (filled circle) α band at 574 nm (circle) in (A) are plotted as a function of L-Trp concentration, and fitted to the Hill equation (solid and dashed line, respectively). (C) The visible region of the absorption spectra of the Y42F mutant upon successive additions of L-Trp. (D) The intensity of the CT1 band at 632 nm in (C) are plotted and fitted to the Hill equation (solid line).

Absorption Spectra of the H76A Mutant

In the absorption spectrum of the ferric H76A mutant, the Soret band was coincident with the position of the Soret band in the wild-type enzyme, while the CT1 band was shifted from 632 nm to 622 nm in the mutant (Fig. 6 B). The resultant spectral features are characteristic of the mixture of high- and low-spin heme irons. It is worth noting that the spectral change in rhTDO induced by the H76A mutation appears similar to the change in the myoglobin (Mb) spectrum induced by the V68D mutation (*65*). The effect of the Mb mutation has been explained by changes in the electrostatic interaction of the heme distal pocket with residue 68. Binding of L-Trp to the ferric H76A mutant leads to a red-shift in the Soret band (from 405 to 407 nm), and a blue-shift in the high-spin β band (from 506 to 503 nm), indicating that L-Trp binding to the active site of the H76A mutant affects both the π-π* transitions and porphyrin skeletal vibrations. The intensity changes of these bands were too small to conduct a quantitative analysis.

Absorption Spectra of the Y42F Mutant

The absorption spectrum of the Y42F mutant shows the Soret band at 407 nm, α/β bands at 584/502 nm, and the CT1 band at 632 nm (Fig. 6 C), This spectrum pattern is similar to that of a wild-type in the absence of L-Trp. The red-shift of the Soret band by 2 nm upon the mutation of Y42F implies that the π-π* transitions of the porphyrin ring are affected by the removal of the OH group. The L-Trp binding to the Y42F mutant alters only the intensity of the absorption bands. The plot of the intensity of the CT1 band of the Y42F mutant exhibits simple saturation kinetics (Fig. 7 C and D), which is in sharp contrast to the sigmoidal behavior of a wild-type enzyme (Fig. 7 B).

Raman Spectra of the Wild-type Enzyme

Fig. 8 shows the resonance Raman spectra of ferric rhTDO in the presence of 0~1 mM of L-Trp. The assignments of the bands, which are described in the spectra, were based on those of ferric Mb (*66*) and rhTDO, as previously reported (*62*) . In the high frequency region of the substrate-free enzyme [Fig. 8 A(a)], the positions of the ν_4 (1,372 cm^{-1}), ν_3 (1,482 cm^{-1}) and ν_2 (1,560 cm^{-1}) bands are essentially identical to those of the corresponding bands of hemoproteins in the six-coordinate high-spin state.

Raman spectral changes were observed upon the addition of L-Trp. In the high-frequency region (Fig. 8 A), the ν_4 band shifted slightly from 1,372 to 1,374 cm^{-1}, and the ν_3 band appeared at ~1,505 cm^{-1}, suggesting an appearance of the heme iron in the six-coordinate, low-spin state. The reduction of the ν_2 peak intensity at 1,560 cm^{-1} is indicative of a six-coordinate, high-spin/low-spin mixture (*67*). In the low-frequency region (Fig. 8 B), the intensity of the γ_6 (pyrrole tilting mode) band at 338 cm^{-1} was reduced, while that of the ν_8 vibration (in-plane skeletal mode) at 350 cm^{-1} increased with the L-Trp concentration. The intensity of the heme propionate bending mode, $\delta(C_\beta C_c C_b)_{6,7}$ at 378 cm^{-1} and 391 cm^{-1}, decreased. The intensity of the heme 4-vinyl bending mode, $\delta(C_\beta C_a C_b)_4$, at 416 cm^{-1}, decreased, although the 2-vinyl bending mode, $\delta(C_\beta C_a C_b)_2$, at 430 cm^{-1}, did not change. The decrease in the intensity of the vinyl stretching mode, ν_{cc}, at 1,625 cm^{-1}, also supports a conformational change in the vinyl group. Because the vinyl stretching vibration, ν_{cc}, and the in-plane skeletal mode, ν_{10}, can overlap at 1,625 cm^{-1}, we measured the polarized resonance Raman spectra of ferric rhTDO (Fig. 9) to determine the depolarization ratio of the Raman band. From the spectra, the polarization ratio of the band at 1,625 cm^{-1} was calculated to be 0.25 and 0.24 in both the absence and presence of L-Trp, respectively. Because the polarization ratio is expected to be 0 and ~0.75 for the ν_{cc} and ν_{10} modes, respectively, the results

show that the ν_{cc} band is the major contributor to the intensity change at 1,625 cm^{-1}.

We analyzed the Raman bands in the 250-450 cm^{-1} region by fitting the data with Gaussian curves. As illustrated in Fig. 10, the deconvolution allowed us to identify nine well-resolved peaks and to detect changes in the intensity of the γ_6, ν_8, $\delta(C_\beta C_c C_b)$ at 378 cm^{-1} and $\delta(C_\beta C_a C_b)_4$ bands. In this analysis, we used the peak area as an indicator of peak intensity. Because the ν_7 mode at 678 cm^{-1} is not significantly affected by either the spin or oxidation states, its intensity was used as a reference to scale the intensity of other modes in each spectrum. The relative intensity of each band was plotted as a function of the L-Trp concentration, as shown in Fig. 11. The plots clearly show the sigmoidal shape for the wild-type rhTDO. Because these conformational changes in the heme reflect the binding of L-Trp to the catalytic sites, the sigmoidal curves imply that the heme conformational change exhibits an allosteric response. The sigmoidicity parameter (Hill coefficient) were estimated as 2.4, 2.7, 2.5 and 2.3 for the γ_6, ν_8, $\delta(C_\beta C_c C_b)$ at 378 cm^{-1} and $\delta(C_\beta C_a C_b)_4$ modes, respectively.

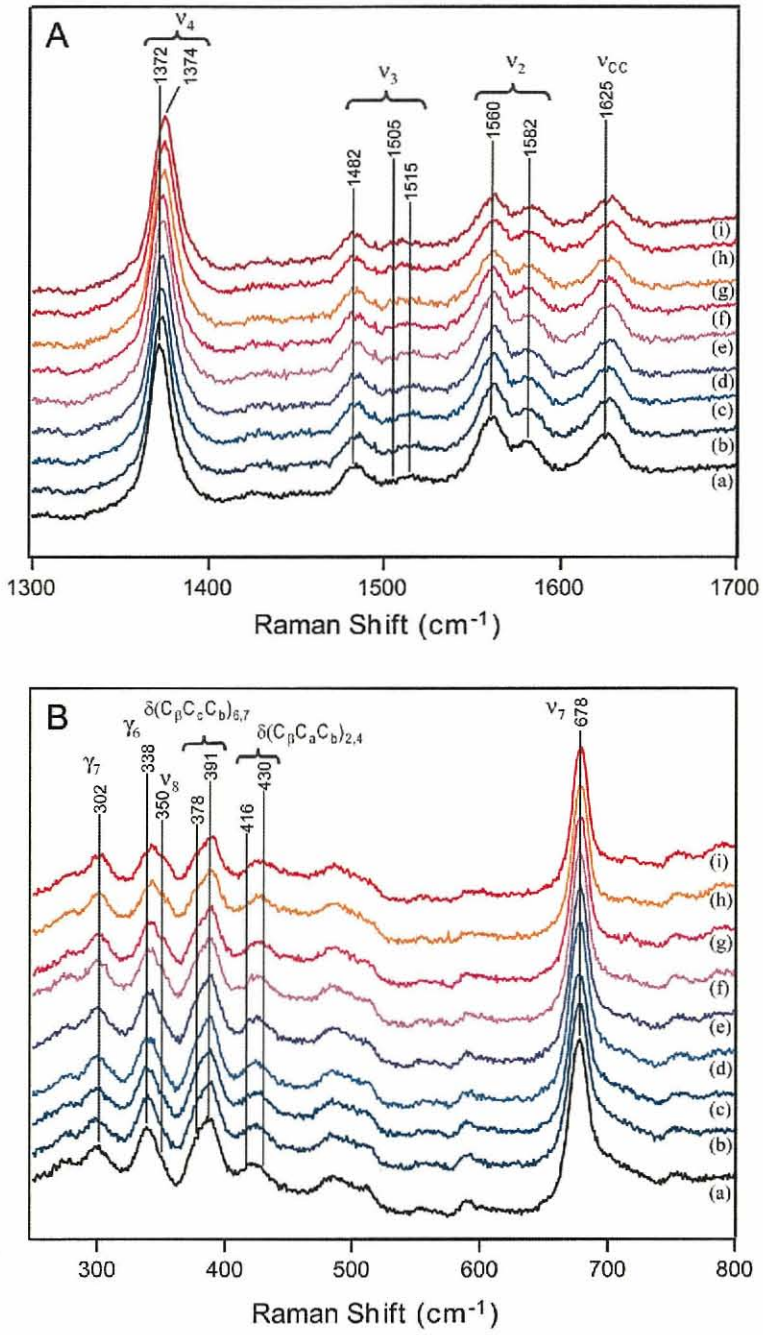

Fig. 8. Resonance Raman spectra of wild-type rhTDO for various L-Trp concentrations.

(A) High-frequency and (B) low-frequency regions are shown. The measurement conditions were as follows: (a) ferric rhTDO without L-Trp, (b) ferric rhTDO + 50 μM L-Trp, (c) ferric rhTDO + 100 μM L-Trp, (d) ferric rhTDO + 200 μM L-Trp, (e) ferric rhTDO + 300 μM L-Trp, (f) ferric rhTDO + 400 μM L-Trp, (g) ferric rhTDO + 600 μM L-Trp, (h) ferric rhTDO + 800 μM L-Trp, (i) ferric rhTDO + 1 mM L-Trp.

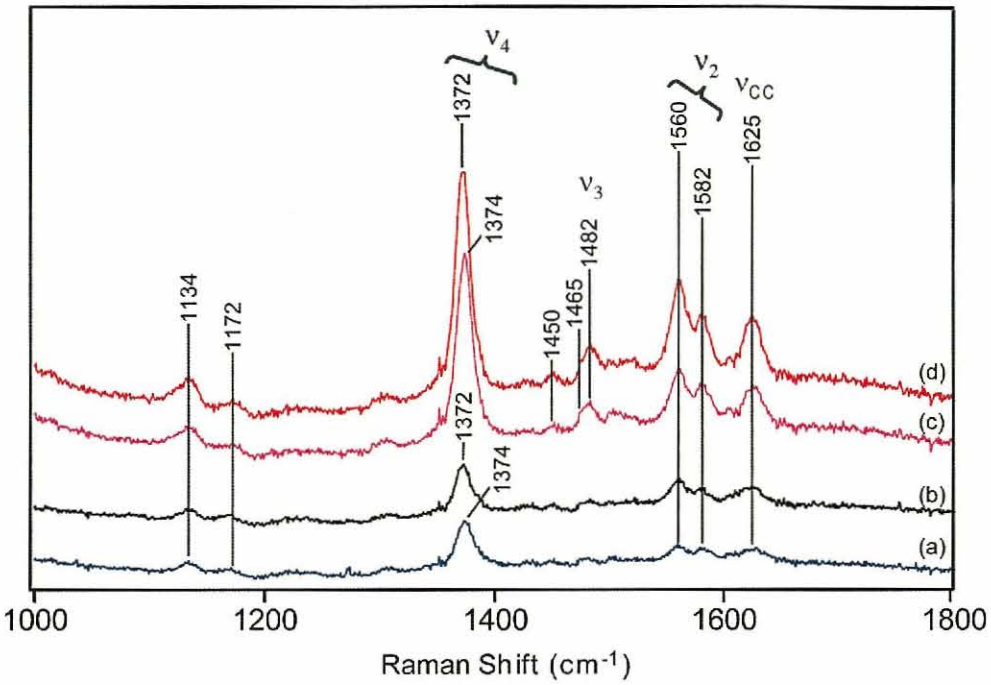

Fig. 9. Polarized resonance Raman spectra of ferric rhTDO.

(a) perpendicular polarization (⊥), ferric rhTDO with 1mM L-Trp, (b) ⊥, ferric rhTDO without L-Trp, (c) parallel (//) polarization, ferric rhTDO with 1 mM L-Trp, (d) //, ferric rhTDO without L-Trp. In the spectra of (a) and (b), only the ν_{10} vibration mode contributes to the peak at 1,625 cm^{-1}. In the spectra of (c) and (d), the ν_{cc} vibration mode contributes to the peak at 1,625 cm^{-1}.

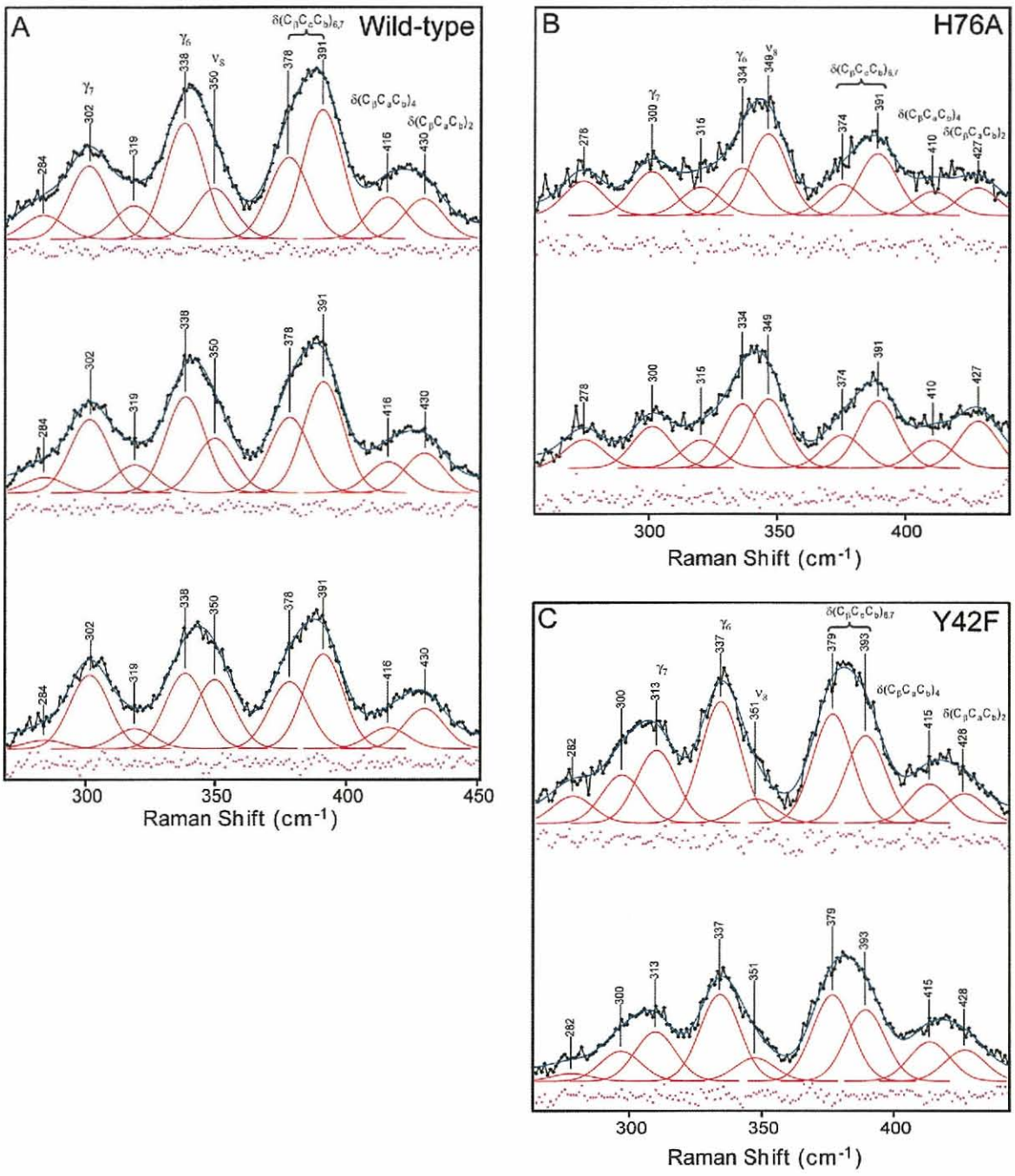

Fig. 10. Deconvolution analysis of Raman bands in the low-frequency region. (A) ferric rhTDO (top) ferric rhTDO + 400 μM L-Trp (middle), ferric rhTDO + 1 mM L-Trp (bottom), (B) ferric H76A mutant (top) and ferric H76A mutant + 2 mM L-Trp (bottom), (C) ferric Y42F mutant (top) and ferric Y42F mutant + 2 mM L-Trp (bottom). The black line with the filled rectangle represents the experimental data. The blue line superimposed on the experimental data represents the calculated data. The nine peaks shown in red are the result of the deconvolution analysis. The dots at the bottom of each spectrum are the residuals from the peak-fitting calculation.

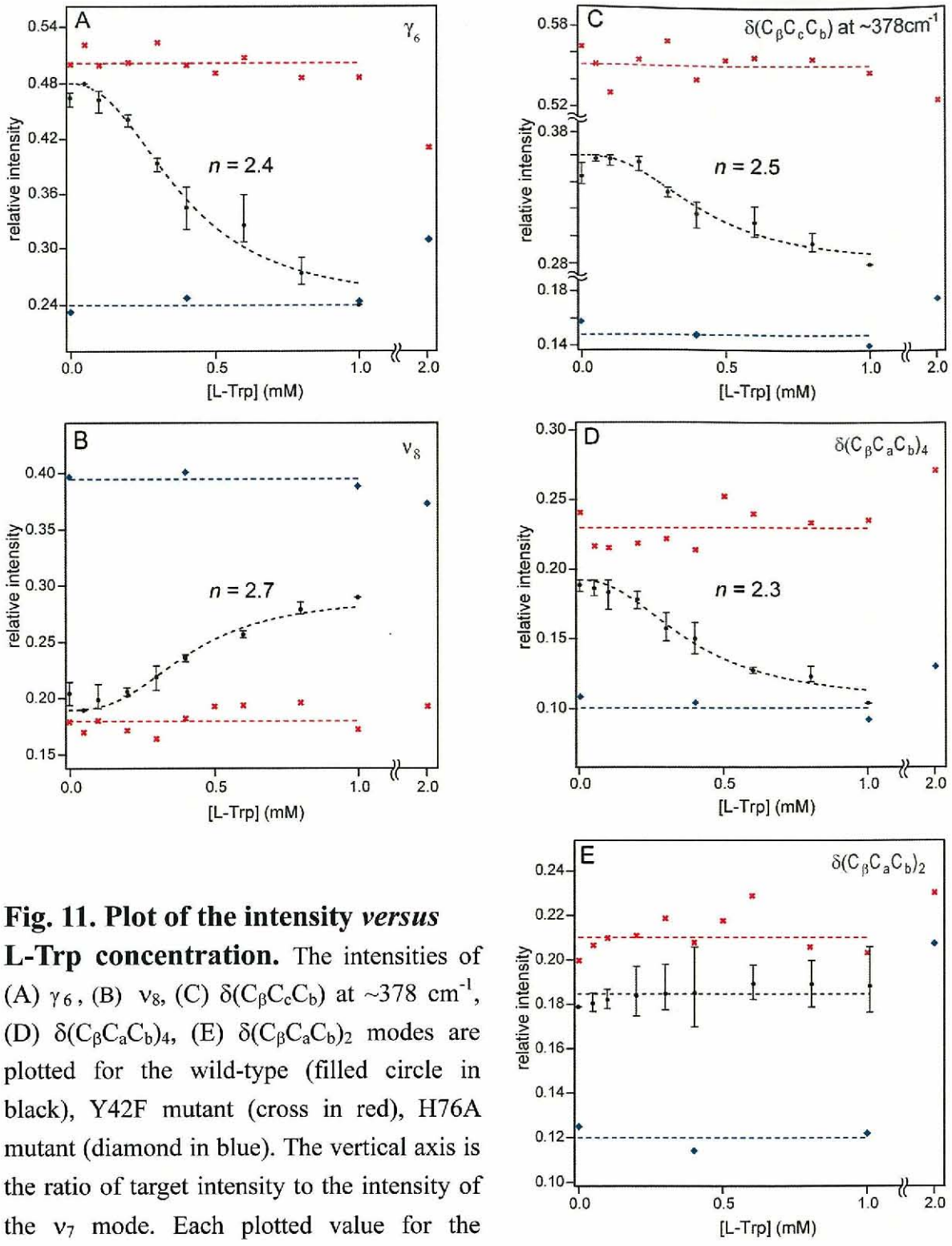

Fig. 11. Plot of the intensity *versus* L-Trp concentration. The intensities of (A) γ_6, (B) ν_8, (C) $\delta(C_\beta C_c C_b)$ at ~378 cm^{-1}, (D) $\delta(C_\beta C_a C_b)_4$, (E) $\delta(C_\beta C_a C_b)_2$ modes are plotted for the wild-type (filled circle in black), Y42F mutant (cross in red), H76A mutant (diamond in blue). The vertical axis is the ratio of target intensity to the intensity of the ν_7 mode. Each plotted value for the wild-type is the mean of triplicate measurements and the error bars indicate minimum and maximum values of three replicates. The dashed lines for the wild-type enzyme are the best-fit curves calculated using Hill equation. Each value plotted for the mutants represents a single measurement. The dashed lines for the mutants indicate the mean of values in 0-1 mM L-Trp.

Raman Spectra of the H76A Mutant

In the high-frequency region of the ferric substrate-free form of the H76A mutant (Fig. 12), the ν_3 band appeared at 1,481 and ~1,507 cm^{-1}, which implies that it adopts a six-coordinate and the high-spin/low-spin mixture, in contrast to the high-spin state of the substrate-free wild-type enzyme. The ν_4 band was slightly down-shifted from 1,373 to 1,372 cm^{-1} by the mutation. As in the wild-type enzyme, the deconvolution analysis of the 250-450 cm^{-1} region showed nine peaks (Fig. 10 B). Because the spin state of ferric H76A in the substrate-free form is different from that of the wild-type, the positions and the intensities of these Raman bands are different. Furthermore, H76A does not show an apparent spin transition upon L-Trp binding, and the mutation considerably reduces the affinity for L-Trp, as supported by a 6-fold increase in the $K_{m(app)}$ value. Therefore, the intensities of ν_8, $\delta(C_\beta C_c C_b)_{6,7}$ and $\delta(C_\beta C_a C_b)_4$ do not change significantly upon the addition (0-2 mM) of L-Trp (Fig. 11 B-D). A small increase in the intensity of both γ_6 vibration at 334 cm^{-1} and $\delta(C_\beta C_a C_b)_2$ vibration at 427 cm^{-1} was detected only when 2 mM L-Trp was used (Fig. 11 A, E). The intensity changes of these Raman bands do not indicate sigmoidal kinetics.

Raman Spectra of the Y42F Mutant

In the high-frequency region of Raman spectra for the ferric substrate-free form of Y42F (Fig. 12), the intensity of the ν_2 band at ~1,557 cm^{-1}, relative to that of 1,576 cm^{-1}, is similar to that of wild-type, which implies that the Y42F mutant predominantly adopts the six-coordinate, high-spin state. After addition of L-Trp, the ν_4 band was slightly down-shifted from 1,372 to 1,371 cm^{-1}, unlike the pattern observed for the wild-type and H76A mutant enzymes. Despite the greater enzyme activity of the Y42F mutant relative to the H76A mutant, addition of L-Trp at concentrations up to 2 mM did

not affect most bands in the 250-450 cm^{-1} region, except for a slight reduction in the γ_6 peak, as shown in Fig. 10 C and 11 A-E. The binding of L-Trp has a very small effect on the spin-state of the heme iron. These results are consistent with the 16-fold increase in the $K_{m(app)}$ value (Table 1).

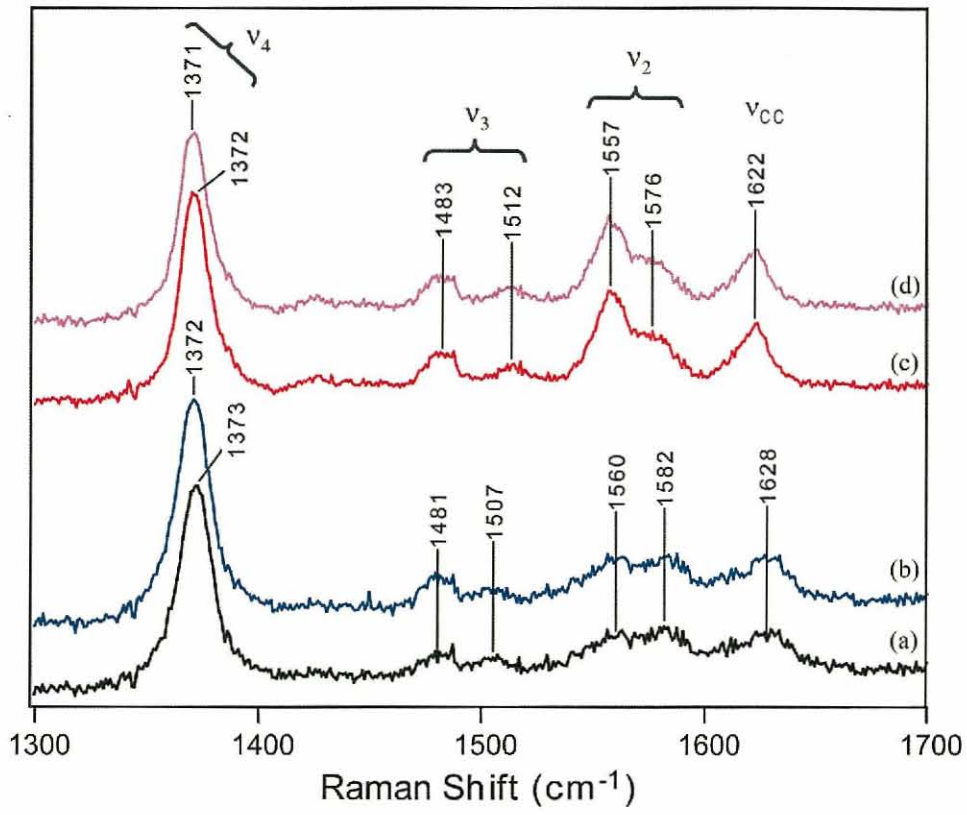

Fig. 12. High-frequency resonance Raman spectra of rhTDO mutants.
(a) ferric H76A mutant, (b) ferric H76A mutant + 2 mM L-Trp, (c) ferric Y42F mutant, (d) ferric Y42F mutant + 2 mM L-Trp.

DISCUSSION

L-Tryptophan Binding to rhTDO

The analysis of substrate binding to ferric rhTDO using resonance Raman spectroscopy has been reported by Batabyal and Yeh (*62*), who compared the spectra of the substrate (L-Trp)-free and -bound enzymes. These results were essentially reproduced in the present study, as shown in Fig. 8. In the present study, we carefully examined the spectral changes of the ferric enzyme during the titration of the substrate, L-Trp. We quantified changes in the peak intensities using deconvolution analysis, which resolved the γ_6 (338 cm^{-1}), ν_8 (350 cm^{-1}), $\delta(C_\beta C_c C_b)_{6,7}$ (378, 391 cm^{-1}) and $\delta(C_\beta C_a C_b)_4$ (416 cm^{-1}) bands in all spectra.

The intensities of the out-of-plane γ_6 mode and the in-plane skeletal ν_8 mode are sensitive to the distortion of the heme plane. Because the Fe atoms are out of the heme plane in the high-spin state, but are in-plane for the low-spin state atoms (*66*), the change of the γ_6 and ν_8 intensities of wild-type rhTDO reflects the mixing the low- to high-spin states upon the L-Trp binding. This result is consistent with the optical spectral data described above. The mixed-spin state indicates that binding of L-Trp to ferric hTDO might facilitate deprotonation of the water that is bound to the sixth coordination position of the heme iron.

Because the heme propionate bending modes, $\delta(C_\beta C_c C_b)_{6,7}$, are sensitive to their environment, the change in their intensity with the elevation of the L-Trp concentration indicates altered H-bonding interactions of the heme propionates upon the L-Trp binding. In addition, the heme 4-vinyl bending mode, $\delta(C_\beta C_a C_b)_4$, which was well-resolved from the 2-vinyl bending mode, $\delta(C_\beta C_a C_b)_2$, in our analysis, decreased in

its intensity upon the L-Trp binding, suggesting a reduction in π-conjugation of the vinyl group with the porphyrin π-system (*68*). A similar change was not observed in the 2-vinyl bending mode of heme. This result suggests that L-Trp binding induces a conformational change only in the 4-vinyl group of the heme.

The conformational changes in the heme of rhTDO induced by the L-Trp binding can be explained on the basis of the crystal structures of bacterial TDO (xTDO), which is homologous to the human enzyme. One of the most striking differences between the substrate-free and L-Trp-bound xTDO was observed at both the 4-vinyl and 7-propionate groups of heme (Fig. 2). In the substrate-free form, the 4-vinyl group is in the in-plane configuration relative to the porphyrin plane, while it adopts the out-of-plane orientation in the substrate-bound form of xTDO. In addition, the bound L-Trp interacts with the 7-propionate group of the heme via its amino group.

With respect to protein interactions, Y24 of xTDO is involved in hydrophobic interactions with the substrate. In addition, the Y24 hydroxyl group has an OH-π interaction with the 4-vinyl group of the porphyrin (Fig. 2), while the OH group of Y24 is displaced toward the C_b atom of the heme 4-vinyl group by 0.7 Å in the L-Trp-bound form. A similar interaction can be expected in rhTDO. The interaction between the conserved Y42 of hTDO and the 4-vinyl group of the heme might be altered by L-Trp binding, causing the heme 4-vinyl group to rotate, thereby altering the intensity of $\delta(C_\beta C_a C_b)_4$ in the Raman spectra. The importance of this interaction for substrate recognition and the heme environment was confirmed by the Y42F mutation that shows considerably lower affinity for L-Trp and only small changes in the optical spectra and Raman band upon addition of L-Trp.

Allosteric Interaction

A novel finding of the present study using spectroscopic methods is that L-Trp binding to rhTDO is sigmoidal, suggesting homotropic allosteric interaction between the subunits of the tetrameric enzymes. By contrast, the enzymatic activity in various L-Trp concentration exhibits simple saturation with Michaelis-Menten kinetics, because further steps (*i.e.* the iron reduction and oxygen binding) are required for the reaction. The anaerobic condition in the titration experiments prevents activation of the enzyme. Activation or later step would limit the overall reaction rate.

Reportedly, NADPH is an allosteric inhibitor of rat liver TDO, which implies the existence of feedback control, as TDO catalyzes the first step in the kynurenine pathway, leading to the formation of NAD (*46*). The compounds, 3-hydroxy anthranilate and α-methyl Trp, which are not substrates for TDO, are also known as heterotropic allosteric modulators (*47*). On the other hand, the study of homotropic allosteric control in mammalian TDO has been limited to the early work of Schutz *et al.*, which showed that cooperative kinetics (Hill coefficient of 1.6) of rat liver TDO were observed only at pH 6.2 and were dependent on both the concentration of L-Trp and the presence of α-methyl Trp (*47*). These data indicate that mammalian TDO possesses two binding sites—a catalytic site and a regulatory site (*7*). Since previous kinetic studies of rat liver TDO and bacterial TDO were based on the rate of product formation in a steady state, it is unknown which step is cooperative and which is rate limiting. On the other hand, the present study demonstrates that the first step of the reaction, L-Trp binding, is a cooperative manner. Although the physiological significance of our results remains to be elucidated, the reaction steps of hTDO in the liver has the potential for regulation by allosteric interaction involving both homotropic and heterotropic mechanisms.

There are two main pathways of Trp metabolism, kynurenine and serotonin pathway.

Internal L-Trp, being an essential amino acid for protein synthesis (4%), is also a precursor of serotonin (1%), but as much as 95% is metabolized via the kynurenine pathway (*69,70*). Serotonin, one of a group of neurotransmitters known as monoamines, is hypothesized to help regulate other neurotransmitter, norepinephrine (noradrenaline) (*71*). Low serotonin levels are believed to be the cause of many cases of mild to severe depression which can lead to symptoms such as anxiety, apathy, fear, feelings of worthlessness, insomnia and fatigue. On the other hand, the excess serotonin activity at central nervous system and peripheral serotonin receptors also produces various specific symptoms. Signs of excess serotonin range from tremor and diarrhea in mild cases to delirium, neuromuscular rigidity, and hyperthermia in life-threatening cases (*72*). Thus, it is important to maintain normal level of serotonin in the body. Conceivably, the cooperativity of TDO might be involved in the mechanism of regulating the flow in two metabolic pathways, depending on the internal concentration of L-Trp, because TDO catalyzes the first and rate-limiting step in kynurenine pathway.

Although the tertiary structure of hTDO remains to be determined, the crystallographic analysis of xTDO might help to reveal the mechanism of cooperativity. The crystal structure of xTDO complexed with L-Trp reveals that two monomers are tightly packed into the asymmetric unit (*31*). The physiological tetramer results from association with the neighboring dimer, which is related by crystallographic two-fold symmetry. The interface between the monomers within the internal dimer is formed by the anti-parallel association of the α2 helices (Fig. 13). The helix α3 of xTDO contributes residues F51 and H55 to the formation of the substrate-binding pocket in the distal region of the heme molecule. Interestingly, both the α1 and α2 helices of xTDO are distal to the core of the polypeptide chain and associate with adjacent subunits in the dimer. In particular, α1 provides Y24 for creation of the substrate-binding pocket in

another chain. Because the amino acid sequence in the region of helices α1, α2, and α3 in TDO is highly conserved among all species (Fig. 3), it can be assumed that TDOs share a common inter-subunit interaction that allows formation of the tetramer. However, whether binding of L-Trp to the catalytic site can regulate the affinity of another catalytic site remains to be determined. We prepared the Y42F mutant of rhTDO to confirm the role of the conserved Tyr residue that forms the catalytic site of the adjacent subunit. As we expected, the Y42F mutant exhibits considerably lower affinity and catalytic activity than the wild-type enzyme. Furthermore, the Y42F mutant abolished the cooperative binding of L-Trp. These data suggest that Y42 is involved in substrate binding in the catalytic site and is responsible for the transmission of the structural change of one active site to an adjacent subunit.

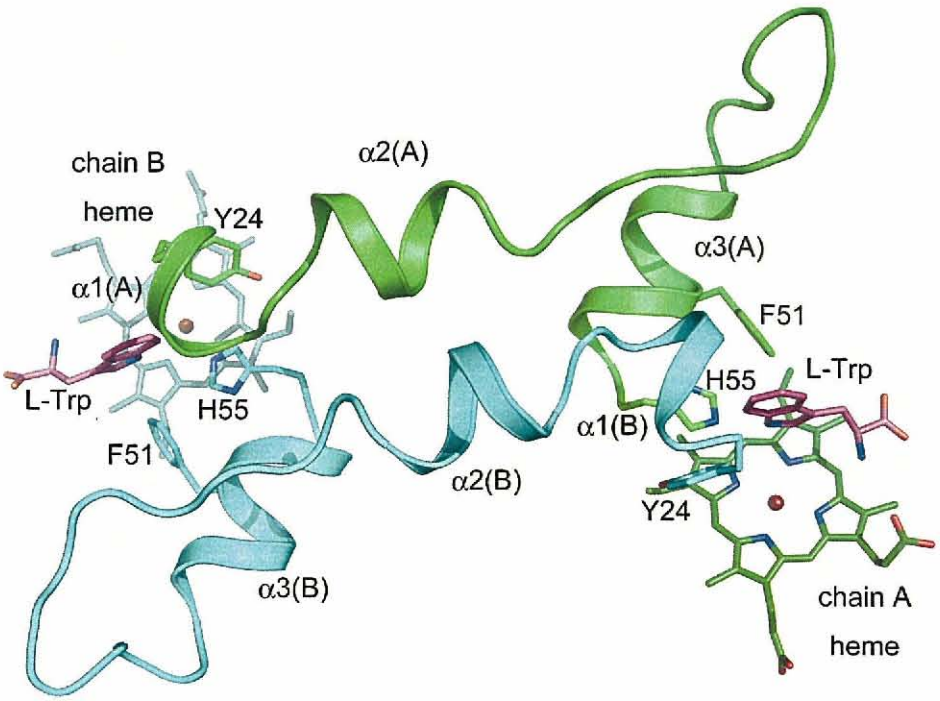

Fig. 13. Interaction of N-terminal helices with adjacent subunit in the tetrameric structure of xTDO.

The structures of the A and B chains are indicated in green and cyan, respectively. The substrate L-Trp is shown in magenta. Y24 of the A chain interacts with the heme in the B chain. Conversely, Y24 in chain B interacts with heme in chain A.

The Reaction Mechanism of Ferric hTDO

As described above, H55 of xTDO and H76 of hTDO play crucial roles in substrate binding, but the role of these residues in catalysis remains to be controversial. Tong and co-workers have suggested that H55 in xTDO is not essential for catalysis, based on results of their biochemical analysis. They found that the $k_{cat(app)}$ of TDO is insensitive to pH over the range examined (pH 6 to 8), and the H55A mutant retained 15% of wild-type activity (*31,58*). On the other hand, Dick and co-workers showed that mutation of this conserved His in recombinant rat TDO significantly reduced the enzymatic activity (*73*). In the present study, we describe the effect of the H76A mutation on the kinetics of hTDO and discuss in detail the importance of the heme environment. The optical absorption spectra and the high-frequency region of the Raman spectra show that the H76A mutant exhibits an increase in the six-coordinate, low-spin state in the ferric form, whereas the ferric wild-type enzyme mostly exists in the six-coordinate, high-spin state. Thus, H76 is involved, either directly or indirectly, in the regulation of the spin state. Additionally, H76 affects the electrostatic field of the heme pocket, as evidenced by the distinctly different CT1 band of the H76A mutant compared with that of the wild-type enzyme.

Although the H76A mutant has only 0.1% of wild-type activity, its $K_{m(app)}$ value is less than that of the Y42F mutant, which has greater activity than H76A. The shift in the optical absorption spectrum and the ν_4 Raman band of H76A after the addition of L-Trp also indicates that the L-Trp binding ability is not fully lost in the H76 mutant. Based on the comparison with bacterial TDO structures, it is likely that H76 of hTDO interacts with the hydrogen of the N1 atom of L-Trp in the catalytic site. Although the present study did not provide direct evidence that H76 acts as a catalytic base for abstraction of a proton from L-Trp, we conclude that H76 of hTDO is important for substrate binding

in the heme pocket as well as for the catalytic reaction.

The rhTDO has a novel characteristic, in which no reducing agent is required for ferric iron to be reduced to its ferrous form when both substrate and molecular oxygen are present. It is also shown that the ferric rhTDO is capable of CO binding without reductant when L-Trp is present (Fig. 14). These observations suggest a ligand-mediated mechanism that enables electron transfer from electron-rich indole to heme iron. Such a reaction might involve the H76 and bring about a catalytically required conformational transition of the enzyme.

Considering our observed data, one possible scenario for the formation of 3-indolenylperoxy intermediate is depicted in Scheme 1. In this mechanism, it is assumed that His 76 acts as a proton donor/acceptor through the hydrogen bond to N1 atom of L-Trp (Scheme 1 i). The base-catalyzed deprotonation of the indole NH group would generate L-Trp anion (Scheme 1 ii). The spin transition from high spin to low spin state with increase of the redox potential, which has been reported in rhTDO (*74*) as well as xTDO (*31*), would have the advantage to accept an electron from L-Trp. The electron transfer event would be coupled to the deprotonation of L-Trp to form neutral radical. After the formation of L-Trp neutral radical and heme reduction (Scheme 1 iii), O_2 then coordinates to the ferrous heme (Scheme 1 iv) and generate the 3-indolenylperoxy intermediate (Scheme 1 v). For conversion of the heme iron-bound 3-indolenylperoxy intermediate to *N*-formylkynurenine, two mechanisms (dioxetane intermediate or Criegee-type rearrangement pathway) are proposed (*31,62*).

In regard to the electron transfer and the formation of Trp neutral radical, similar mechanism has been proposed for the reaction of the autocatalytical hydroxylation by lignin peroxidase (*75*). The reaction involves the electron transfer pathway between Trp residue and nearby heme to form neutral Trp radical that is followed by the insertion of

oxygen into the C3 position. In another case, the calculation based on the structure of versatile peroxidase also indicates the formation of Trp neutral radical as a transition state (*76*). In the case of hTDO, the abstraction of proton from N1 by His76 would be a trigger for the electron transfer from L-Trp to the heme group. However, due to very low acidity of indole NH bond (pKa = 16 in aqueous solution) (*77*), the reaction initiated by the abstraction of proton is not considered to be feasible event in normal environment. The effects of proteins, namely, electrostatic and steric interactions between the substrate and active site residues will be the interesting topic of our future crystallographic study.

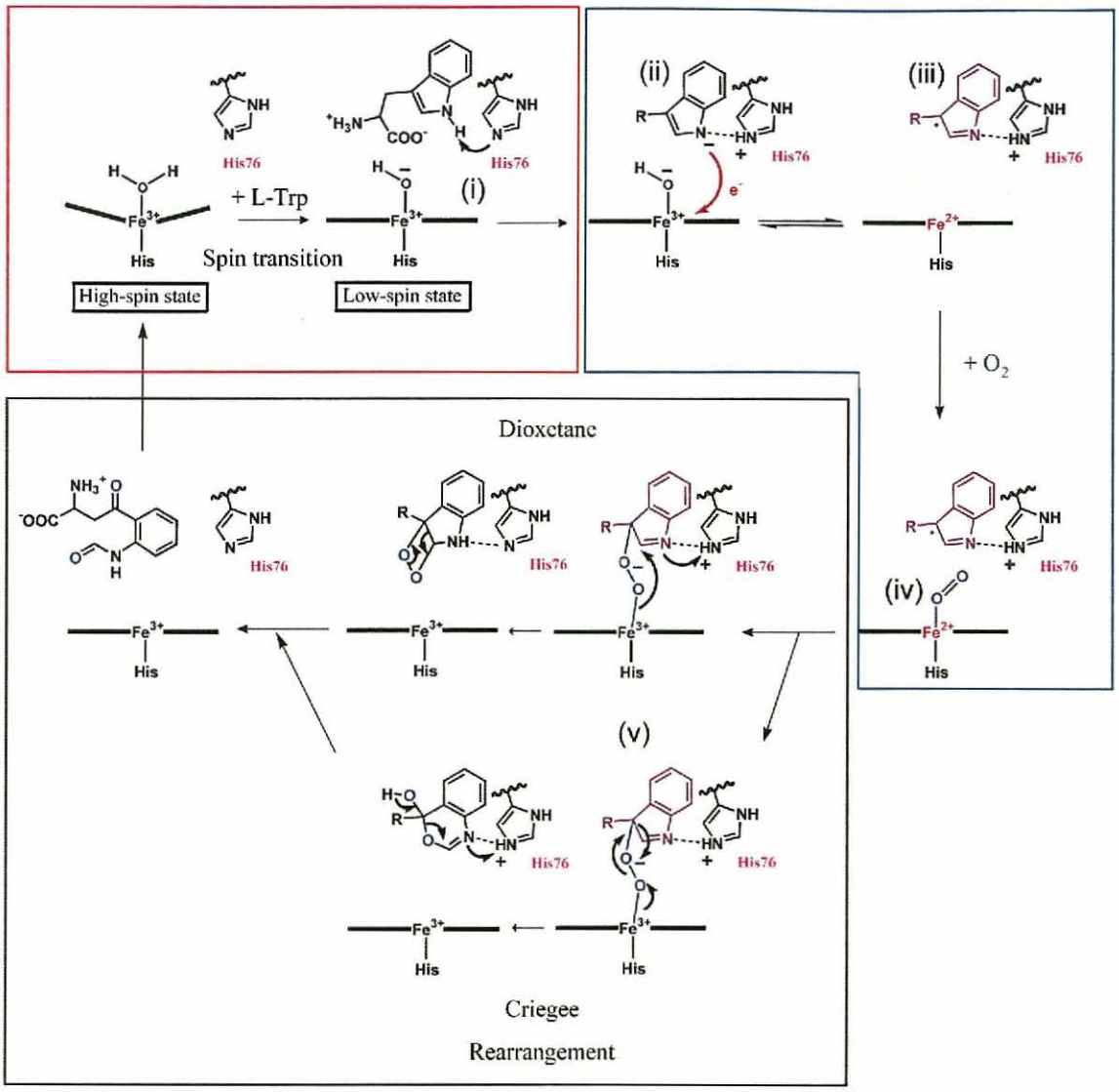

Scheme 1. The proposed reaction for the oxidation of tryptophan by ferric hTDO. A part surrounded by a red border indicates the mechanism reflected in the results of resonance Raman spectroscopic study and mutants analysis on rhTDO. A part surrounded by a blue border indicates the predictable way to produce the oxy-form. A part surrounded by a black border indicates the reactions between L-Trp neutral radical and an oxygen molecule bound to ferrous heme based on the two mechanisms postulated before (dioxetane and Criegee rearrangements).

(i) The deprotonation of the N-1 indole proton. (ii) The electron transfer from L-Trp anion to heme iron. (iii) The formation of L-Trp neutral radical. (iv) O_2 coordination to the ferrous heme. (v) The generation of the 3-indolenylperoxy intermediate.

The electron transfer and ferrous heme are shown in red. L-Trp neutral radical and oxygen atoms are shown in purple and blue, respectively.

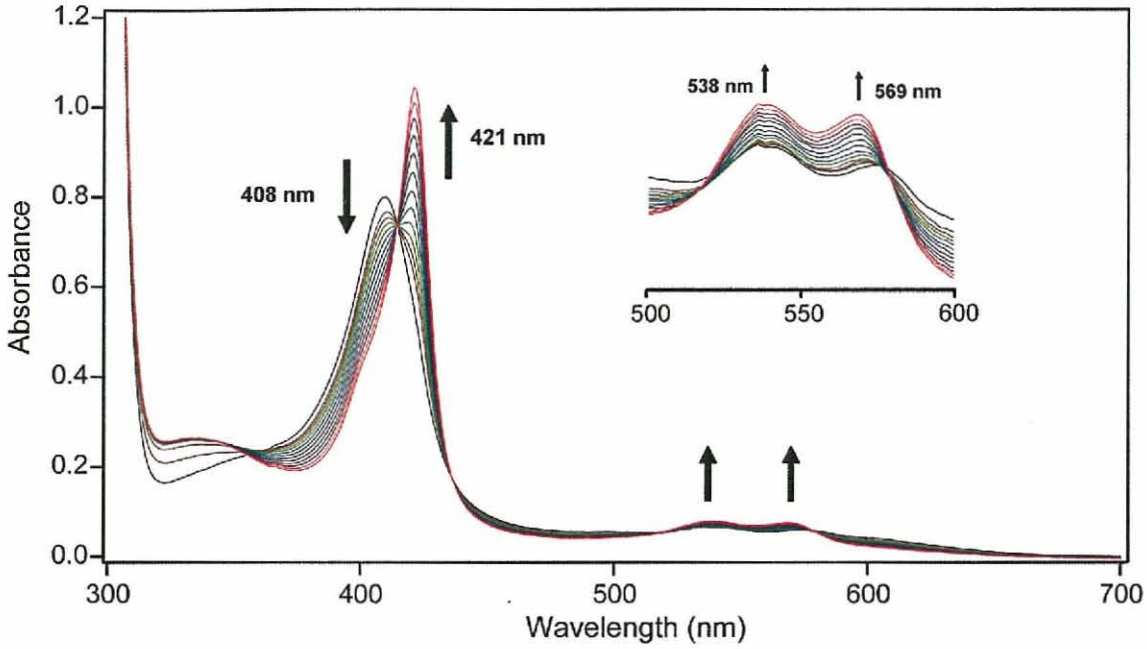

Fig. 14. Change in the absorption spectra of ferric rhTDO with L-Trp under CO atmosphere at 25°C.

Arrows indicate the direction of change in absorbance upon successive additions of CO. The spectra were taken at the beginning of the reaction and then after each 1 min for 12 min. Buffer conditions: 50 mM potassium phosphate pH8.0, 200 mM NaCl.

CHAPTER II

Crystallization of Human Tryptophan 2,3-Dioxygenase

SUMMARY

Tryptophan 2,3-dioxygenase (TDO) is a heme-containing dioxygenase and catalyzes the oxidative cleavage of the pyrrole ring of indoleamines by the insertion of molecular oxygen. This reaction is the first and the rate-limiting step in the kynurenine pathway, the major Trp catabolic pathway in mammals. The recombinant human TDO (rhTDO) was crystallized by the vapour diffusion technique. Because the diffraction pattern of the initially obtained crystals was not suitable for structure analysis, the enzyme was engineered by optimizing the length of truncation in N-terminal amino acid sequence, and type of affinity tag (*eg.* hexahistidine, maltose-binding protein, or glutathione-*S*-transferase tag) to increase the stability and chance of crystallization. The solubility of rhTDO was enhanced when N-terminal 35 residues were truncated and hexahistidine tag was added in its N-terminal. The best crystal was obtained using this construct and the reservoir solution contains 10% (w/v) PEG 6,000, 100 mM Tri-potassium citrate and 20 mM HEPES pH 7.0. The addition of 4-phenylimidazole as a heme ligand was also essential for the crystallization. The crystals diffract to 8 Å resolution using synchrotron radiation and belong to space group $P2_1$ with unit cell parameters of a = 93.1 Å, b = 134.3 Å, c = 125.9 Å and b = 91.6°. Matthews coefficient (V_m) calculation suggests two tetramers are present in the asymmetric unit with solvent content of 44% (V_m = 2.2).

MATERIALS AND METHODS

Construction of Expression Plasmids

N-terminal Deletion Mutants of rhTDO

The secondary structure of hTDO was predicted with PSIPRED (Fig. 1). PSIPRED is a program developed by David Jones, which predicts protein secondary structure using the position specific scoring matrices generated by PSI-BLAST. The N-terminal sequence up to I41 of hTDO was predicted as a coiled-coli structure. Consequently, three types of truncated mutants, hTDO-ΔN40, hTDO-ΔN35 and hTDO-ΔN15 were designed to get more stable protein. For the plasmid for hTDO-ΔN40, the cDNA encoding full-length hTDO was amplified by PCR using a forward primer hTDO-ΔN40-*Nde*I (Table 1 A) which contains the *Nde*I site followed by the coding sequence of hTDO starting at I41, and a reverse primer, hTDO-*Bam*HI (Table 1 B). For hTDO-ΔN35, the forward primer hTDO-ΔN35-*Nde*I (Table 1 C) which contains the *Nde*I site and coding sequence of hTDO starting at S36, and the same reverse primer were used. The PCR product was digested by restriction enzymes and ligated into pET-15b vector at *Nde*I and *Bam*HI sites. The preparation of hTDO-ΔN15 plasmid was described in chapter I.

MBP-tagged hTDO-ΔN15 and MBP-tagged hTDO-ΔN35

The plasmid for expression of MBP and hTDO-ΔN15 fusion protein, the hTDO cDNA was amplified by PCR using a forward primer hTDO-ΔN15-*Kpn*I (Table 1 D), which contains the *Kpn*I site followed by coding sequence of hTDO starting at K16, and a reverse primer, hTDO-*Bam*HI (Table 1 B). The PCR product was ligated into the *Kpn*I/*Bam*HI sites of the MBP-expression vector pMAL-c2E (New England Biolabs). The sequences encoding Pro which is a part of the *Kpn*I site was mutated into Ser using QuikChange site-directed mutagenesis kit (Stratagene) with pMAL-c2E hTDO-ΔN15 as a template. Similarly, pMAL-c2E hTDO-ΔN35 was also constructed: the hTDO cDNA was amplified by PCR using a forward primer hTDO-ΔN35-*Kpn*I (Table 1 E) which contains *Kpn*I site followed by the coding sequence starting at Met connected to S36, and the same reverse primer as using for construction of pMAL-c2E hTDO-ΔN15 (Table 1 B).

pMAL-c2E hTDO-ΔN15 plasmid was further modified because the presence of the flexible linker in the expressed protein may prevent stable association of the fusion partners (*78*). The modifications of amino acids in the MBP fusion protein contain the substitution of the 25-amino acid linker with only three alanine residues, and the mutation of charged residues near the C-terminus of MBP to alanines. A gene fragment encoding a mutated version of MBP was generated by PCR using the primer pair of MBP-*Bgl*II (Table 1 F) and MBP-*Pvu*II (Table 1 G), and pMAL-c2E as the template. The MBP-*Pvu*II primer is designed to introduce additional substitutions of E359A, K362A and D363A in MBP, and to mutate SSS sequence at linker region (*Sac*I site) into AAA sequence (*Pvu*II site) to favor helix extension. The DNA fragment for hTDO-ΔN15 was amplified using the primer pair hTDO-ΔN15-*Pvu*II (Table 1 H) and the reverse primer hTDO-*Bam*HI (Table 1 B). The two PCR products were then ligated

simultaneously into the *Bgl*II-*Bam*HI sites of pMAL-c2E.

GST-tagged hTDO-ΔN15 and GST-tagged hTDO-ΔN35

The plasmids for GST fusion protein were created using pFN2A Flexi vector (Promega). To construct GST-tagged hTDO-ΔN15, the hTDO cDNA was amplified by PCR using a forward primer, hTDO-ΔN15-*Sgf*II (Table 1 I), which contains *Sgf*II site followed by the coding sequence of hTDO starting at K16, and a reverse primer, hTDO-*Pme*I (Table 1 J). The PCR product was digested by restriction enzymes and ligated into pFN2A at the *Sgf*I and *Pme*I sites, which creates pFN2A hTDO-ΔN15 encoding the fusion construct with GST at the N-terminus of the hTDO-ΔN15 and a TEV protease recognition sequence to allow cleavage and removal of GST. Similarly, pFN2A hTDO-ΔN35 was also constructed as follows: The hTDO cDNA was amplified by PCR using a forward primer, hTDO-ΔN35-*Sgf*I (Table 1 K), which contains *Sgf*I site followed by hTDO sequence starting at S36, and same reverse primer as used for the construction of pFN2A hTDO-ΔN15. The PCR product was digested by restriction enzymes and ligated into pFN2A at the *Sgf*I and *Pme*I sites to generate the pFN2A hTDO-ΔN35. Furthermore, the coding region of the GST fused to truncated mutant of hTDO in the pFN2A hTDO-ΔN15 was amplified by PCR using forward primer, GST-*Nde*I (Table 1 L) and the above reverse primer (Table 1 B). This amplified fragment was directly ligated to *Nde*I/*Bam*HI-digested pET15b with a hexa-histidine tag and a thrombin site fused to the N-terminus of GST, to produce pET15b GST_hTDO-ΔN15. The plasmid of pET15b GST_hTDO-ΔN35 was similarly prepared.

```
Conf: 999989996100257888777777846457766756897599998079898566755555
Pred: CCCCCCCCCCCCCCCCCCCCCCCCCCCCCCCCCCCCCCCCCCCCHHHHHHHHHHHHCCCCCCC
hTDO: MSGCPFLGNNFGYTFKKLPVEGSEEDKSQTGVNRASKGGLIYGNYLHLEKVLNAQELQSE
              10        20        30        40        50        60

Conf: Confidence (0=low, 9=high)
Pred: Predicted secondary structure (H=helix, E=strand, C=coil)
```

Fig 1. PSIPRED prediction result of hTDO N-terminal sequence.

Table 1. Primer sequences used for amplification.

primer	Sequence (5' to 3')
(A) hTDO-ΔN40-*Nde*I	GGGCATATGATCTATGGGAACTACCTGCATTTGG
(B) hTDO-*Bam*HI	GGGGATCCTTAATCTGATTCATCACTGCTGAAG TAGG
(C) hTDO-ΔN35-*Nde*I	GGGCATATGAGCAAAGGAGGTCRRATCTATGG
(D) hTDO-ΔN15-*Kpn*I	GGGGTACCGATGAAAAAACTCCC
(E) hTDO-ΔN35-*Kpn*I	GGGGTACCGATGAGCAAAGGAGGTCTTATCTATGG
(F) MBP-*Bgl*II	CTGATTTATAACAAAGATCTGCTGCCG
(G) MBP-*Pvu*II	GTTGTTTACGCAGCTGCATTAGTCTGCGC***GGCTGC***CA GGGC***TGC***ATCGACAGTC
(H) hTDO-ΔN15-*Pvu*II	GGGATTGCAGCTGCGATGAGTAAAAAACTCCC
(I) hTDO-ΔN15-*Sgf*I	AGGAGCGATCGCCATGAAAAAACTCCCCGTAGAAGG
(J) hTDO-*Pme*I	GGTTGTTTAAACTTAATCTGATTCATCACTGCTG
(K) hTDO-ΔN35-*Sgf*I	AACTGCGATCGCCATGAGCAAAGGAGGTCTTATC
(L) GST-*Nde*I	GGGCATATGTCCCCTATACTAGG

[a]Restriction sites are underlined.

[b]Mutated sequences of MBP are bold italic.

Expression and Purification of Truncated Mutants of hTDO

The truncated mutants (hTDO-ΔN40, hTDO-ΔN35 and hTDO-ΔN15) are expressed in *E. coli* and purified using the same protocol for hTDO-ΔN15 as described in chapter I. Expressed protein was purified in several ways adapted to each construct. However, in the crystallization in 4PI form, the buffer containing 5 mM 4PI was used from fracture of cell pellets in the stage of purification. All His-tagged hTDO expressed using the constructs on the basis of the pET15b vector purified as described in chapter I.

Purification of MBP-tagged hTDO

Frozen cell pellets were resuspended in 120 mL of lysis buffer (20 mM Tris-HCl (pH 8.0), i.e., buffer A) containing EDTA-free complete protease inhibitor cocktail tablets (Roche), lysozyme (0.1 mg/ml), and DNaseI (0.01 mg/ml), followed by stirring for 1 h. Cells were lysed by sonication, and the cell debris was removed by ultracentrifugation at 185,000 × *g* for 30 min at 4°C. The resulting supernatant was loaded onto an Amylose Resin (New England Biolabs) column that had been equilibrated with lysis buffer supplemented with 200 mM NaCl (buffer B). The column was washed with the same buffer, and MBP-tagged protein was eluted from the column using the same buffer containing 10 mM maltose (buffer C). The collected proteins were then dialyzed against buffer B overnight at 4°C. The dialyzed proteins were concentrated and further purified using a Superdex-200 size-exclusion column with buffer B. The fractions that contained molecules similar in size to tetrameric MBP-tagged hTDO were pooled, and concentrated using Amicon Ultra-15 centrifugal filter devices (Millipore) containing a cellulose filter with a 50-kDa cutoff. After concentration of the fractions, the solution was filtered with a 0.22-μm disposable filter.

Purification of GST-tagged hTDO

Frozen cell pellets were resuspended in 120 mL of lysis buffer (4.3 mM Na_2HPO_4, 1.47 mM KH_2PO_4, i.e., buffer D) containing EDTA-free complete protease inhibitor cocktail tablets (Roche), lysozyme (0.1 mg/ml), and DNaseI (0.01 mg/ml), followed by stirring for 1 h. Cells were lysed by sonication, and the cell debris was removed by ultracentrifugation at 185,000 × *g* for 30 min at 4°C. The resulting supernatant was loaded onto a GST•Bind resin (Novagen) column that had been equilibrated with lysis buffer supplemented with 137 mM NaCl and 2.7 mM KCl [buffer E (pH 7.3)]. The column was washed with the same buffer, and GST-tagged proteins were eluted from the column using the elution buffer (50 mM Tris-HCl (pH 8.0) containing 10 mM reduced glutathione, i.e., buffer F). The eluted proteins were then dialyzed against buffer F containing 200 mM NaCl without reduced glutathione (buffer G) overnight at 4°C. The dialyzed protein was concentrated and further purified using a Superdex-200 size-exclusion column with buffer G. The fractions that contained molecules similar in size to tetrameric GST-tagged hTDO were pooled, and concentrated using Amicon Ultra-15 centrifugal filter devices (Millipore) containing a cellulose filter with a 50-kDa cutoff. After concentration of the fractions, the solution was filtered with a 0.22-μm disposable filter.

Crystallization of Recombinant Human TDO

Initial Crystallization Screening

For the initial screening of crystallization conditions, commercially available kits listed in Table 2 (except for No. 6) were used. Crystallization trials of rhTDOs were performed using sitting-drop vapour-diffusion method (*79*) at 20°C, with 2 μl drops containing 1 μl 20 mg/ml protein and 1 μl reservoir solution.

Improvement of Crystals

The initial conditions that hit crystal were optimized by varying the precipitants, the additives (No. 6 in Table 2), pH values, temperature and the protein concentration. These optimizations were carried out using hanging-drop vapour-diffusion method (*79*). The droplet was made by mixing 1.5~2 μl protein solution and 1.5~2 μl reservoir solution. Each hanging drop was equilibrated against a 500 μl reservoir solution. Additionally, microseeding method (*80*) and an oil layer consisting of 50% (v/v) paraffin and 50% (v/v) silicon deposited over the surface of the reservoir solutions were used in order to avoid the crystals growing together and reduce the vapour-diffusion rate (*81*). The seed preparations were made using the 'Seed Bead' kit from Hampton Research. Crystals were placed in 50 μl of their respective reservoir solution and mechanically homogenized on a standard laboratory vortex for 3 min at full speed. Dilutions of the seed stocks (between 1×10^{0} and 1×10^{-4}) were also made with the respective reservoir solutions. To obtain the crystals in ferrous state, the protein was reduced by the addition of sodium dithionite, and all steps were performed at 18°C in a glove box with the O_2 concentration maintained < 5 ppm.

Table 2. Crystal screening kits used in this study.

No.	*Product name*	*Screen size*	*Manufacturer*
1	Crystal Screen	50	Hampton Research
2	Crystal Screen 2	48	Hampton Research
3	Crystal Screen Lite	48	Hampton Research
4	PEG/Ion Screen	48	Hampton Research
5	MembFac	48	Hampton Research
6	Additive Screen I~III	24×3	Hampton Research
7	Wizard I・II	48×2	Emerald Biostructures
8	Cryo I・II	48×2	Emerald Biostructures
9	JB Screen classic 1~10	24×10	Jena Bioscience
10	MemStart	48	Molecular Dimensions
11	MemSys	48	Molecular Dimensions
12	JCSG Core Suite I~IV	96×4	Qiagen

X-ray Diffraction Experiments

The crystals were soaked in reservoir solution in a stepwise fashion finally containing 25% ethylene glycol. Crystals were picked up with nylon-fibre loops and flash-cooled in a nitrogen-gas stream. When the crystals were obtained in anaerobic condition, the crystals were soaked in cryoprotectant and flash-cooled inside the glove box in liquid nitrogen.

The quality of the crystals was checked by X-ray diffraction experiments on BL44B2 at SPring-8 (Harima, Japan). The X-ray diffraction data set was collected on BL41XU at SPring-8. The diffraction data were indexed, integrated and scaled with the *HKL*-2000 program package (*82*).

RESULTS AND DISCUSSION

Since N-terminal sequence analysis of the purified full-length rhTDO revealed the N-terminal proteolytic truncation sites as described in chapter I, the series of truncated mutants were designed for crystallization. Table 3 shows total 10 different constructs of rhTDO that were expressed in *E. coli* and purified. The purified protein was used for the initial screening of crystallization condition. Various commercially available screening kits (Table 2) were used for reservoir solution in the vapour-diffusion method (*79*). The protein solutions in the presence of ligand for heme (4PI or CN^-) or substrate (L-Trp) were also used for screening. As described below, three types of N-terminal truncated mutants of rhTDO showed initial crystal hits, while MBP- or GST-fusion constructs of rhTDO yielded no crystal at all.

rhTDO-ΔN15 was expressed as a His-tag fusion protein and the His-tag removed by thrombin in the purification. Screening for rhTDO-ΔN15 in the presence of 4PI yielded the thin plate-like crystal covered with small clusters (Fig. 2 A) in the solution No. 17 of MembFac (100 mM sodium chloride, 100 mM sodium citrate tribasic dehydrate pH 5.6, 12% (w/v) polyethylene glycol (PEG) 4,000 produced at 20°C. Since this crystal did not diffract X-ray, the reservoir condition was optimized to 100 mM tri-pottasium citrate, 100 mM MES pH 6.3, 10% (w/v) PEG 4,000 supplemented with one-tenth of the volume of 15% (w/v) 1,2,3-Heptanetriol (Additive Screen 1, No.19) at 20°C (Fig. 2 B). The diffraction of this crystal was very weak and its highest resolution was limited to ~7 Å (Fig. 3 A). Micro-seeding technique enabled rhTDO-ΔN15 to be crystallized under another reservoir condition of 100 mM tri-sodium citrate, 100 mM potassium phosphate pH 7.0, 12% (w/v) PEG 8,000 at 20°C (Fig. 2 C). The problem of stacking of multiple

crystals during crystal growth was partly resolved but the crystal was still very thin plate. X-ray diffraction of this crystal was highly anisotropic (Fig. 3 B). The attempt to slow down the crystal growth by covering the surface of the reservoir solution by the oil layer had little effect on the thickness of the crystal, and the lowering temperature below 10°C resulted in protein precipitation.

In the preparation of rhTDO-ΔN40, the His-tag at N-terminus was retained because it could not be cleaved by thrombin. The enzyme maintains the activity and tetrameric assembly. The plate-like single crystals of His-tagged rhTDO-ΔN40 were obtained in reservoir condition of 100 mM tri-potassium citrate, 20 mM HEPES pH 7.0 and 10% (w/v) PEG 8,000 at 20°C (Fig. 2 D). The reflection was still weak, and the diffraction was limited to ~8 Å resolution (Fig. 3 C).

rhTDO-ΔN35 was also expressed as a His-tag fusion protein and the His-tag was removed by thrombin cleavage. The plate-like single crystal of rhTDO-ΔN35 with 4PI was obtained in reservoir condition of 100 mM tri-potassium citrate, 20 mM HEPES pH 7.0 and 10% (w/v) PEG 6,000 at 20°C (Fig. 2 E). The crystal grew to maximum dimensions of 100 μm × 150 μm × ~20 μm in a week and diffracted to 8 Å resolution (Fig. 3 D). X-ray diffraction data were collected on BL41XU at SPring-8. The crystals belong to monoclinic system with unit-cell parameters a = 93.1 Å, b = 134.3 Å, c = 125.9 Å and β = 91.6° (Table 4). The systematic absence on 0 k 0 axis of reciprocal lattice indicates a space group $P2_1$. Matthews coefficient (V_m) calculation suggests two tetramers are present in the asymmetric unit with solvent content of 44% (V_m = 2.2).
The low resolution of X-ray diffraction data prevented from determining the tertiary structure of hTDO. One of the main problems in the crystallization of hTDO is the liquid-liquid phase separation. Commonly used crystallizing agents (*e.g.* salt, PEG) and physicochemical parameters (*e.g.* temperature, pressure, pH) can lead to several undesirable metastable phase separations: liquid-liquid phase separation, aggregation

and gelation are the most common type. Metastable states can affect protein crystallization but their positive and negative effects are only partially understood. Another problem is anisotropic diffraction, in which packing in two directions is well-ordered, but stacking of layers in the third dimension is less regular. Loose packing of molecules might result in low-resolution and poor-quality diffraction. Although the truncation of 35 residues in N-terminal of rhTDO improved the enzyme stability and led to the crystallization, further mutagenesis of surface residues to form better packing interactions would be needed for improvement of crystalline quality. In addition, presence of heterotropic allosteric modulators of hTDO (*e.g.* NAD) or factors to eliminate conformational heterogeneity might be effective for crystal quality.

Table 3. Produced fusion proteins and the results of crystallization.

Fusion protein	*Affinity tag*	*Linker or cleavage site*	*Removal of tag*	*Crystallization*
6×His/ hTDO-ΔN15	6×His	thrombin site	○	○
6×His/ hTDO-ΔN35	6×His	thrombin site	○	○
6×His/ hTDO-ΔN40	6×His	thrombin site	×	○
MBP/ hTDO-ΔN15	MBP (TVDEALKDAQTN)	S_3N_{10}LGIEGRISEFGS	×	×
MBP/ hTDO-ΔN35	MBP (TVDEALKDAQTN)	S_3N_{10}LGIEGRISEFGS	×	×
mutated MBP/ hTDO-ΔN15	MBP (TVD***A***AL***AA***AQTN)	AAA	×	×
GST/ hTDO-ΔN15	GST	TEV protease site	×	×
GST/ hTDO-ΔN35	GST	TEV protease site	×	×
6×His/GST/ hTDO-ΔN15	6×His, GST	thrombin site for 6×His, TEV protease site for GST	only 6×His	×
6×His/GST/ hTDO-ΔN35	6×His, GST	thrombin site for 6×His, TEV protease site for GST	only 6×His	×

[a] The parenthetical sequences indicates the C-terminal helix of MBP. The mutations of MBP are highlighted in bold italic.

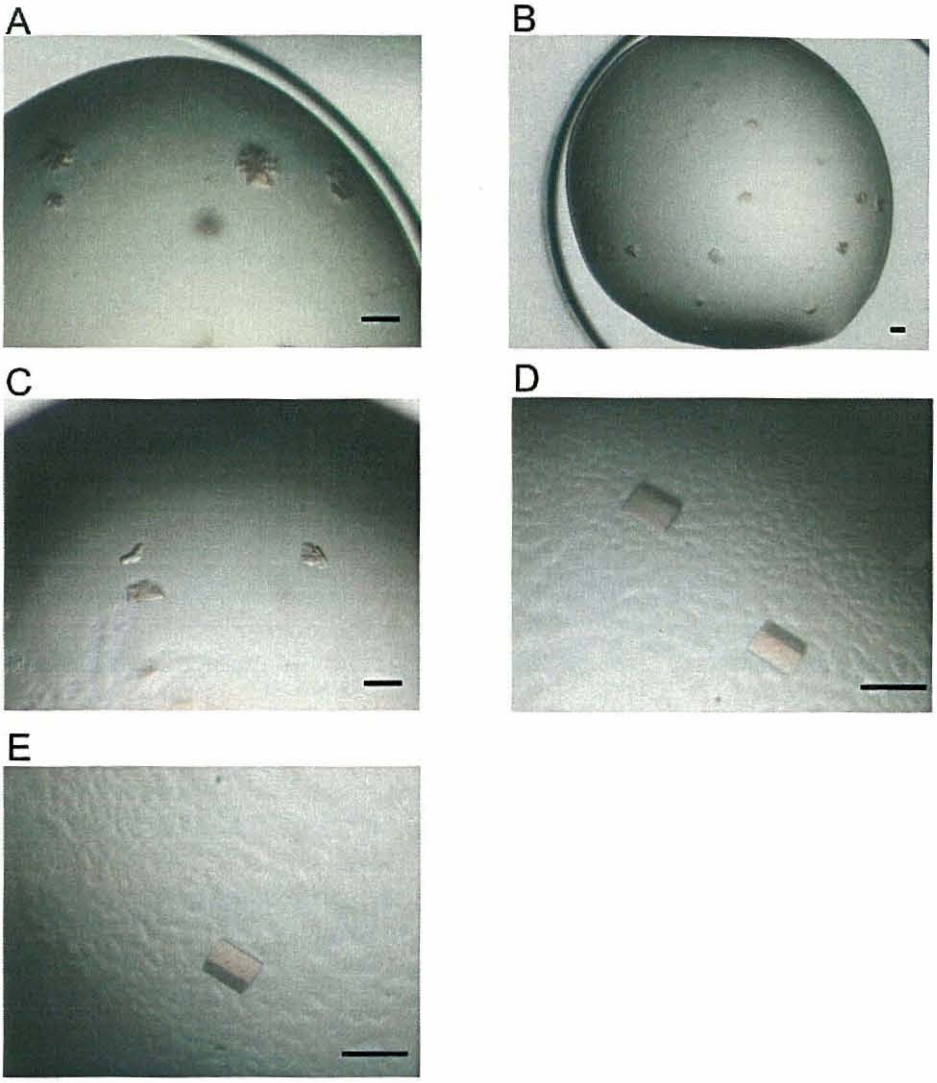

Fig 2. rhTDO crystals.

The scale bars indicate 0.2 mm.

(A) Initial crystals of rhTDO-ΔN15 crystals. (B) Optimized rhTDO-ΔN15 crystals using Additive Screen. (C) rhTDO-ΔN15 crystals produced by microseeding method. (D) rhTDO-ΔN40 crystals. (E) rhTDO-ΔN35 crystals.

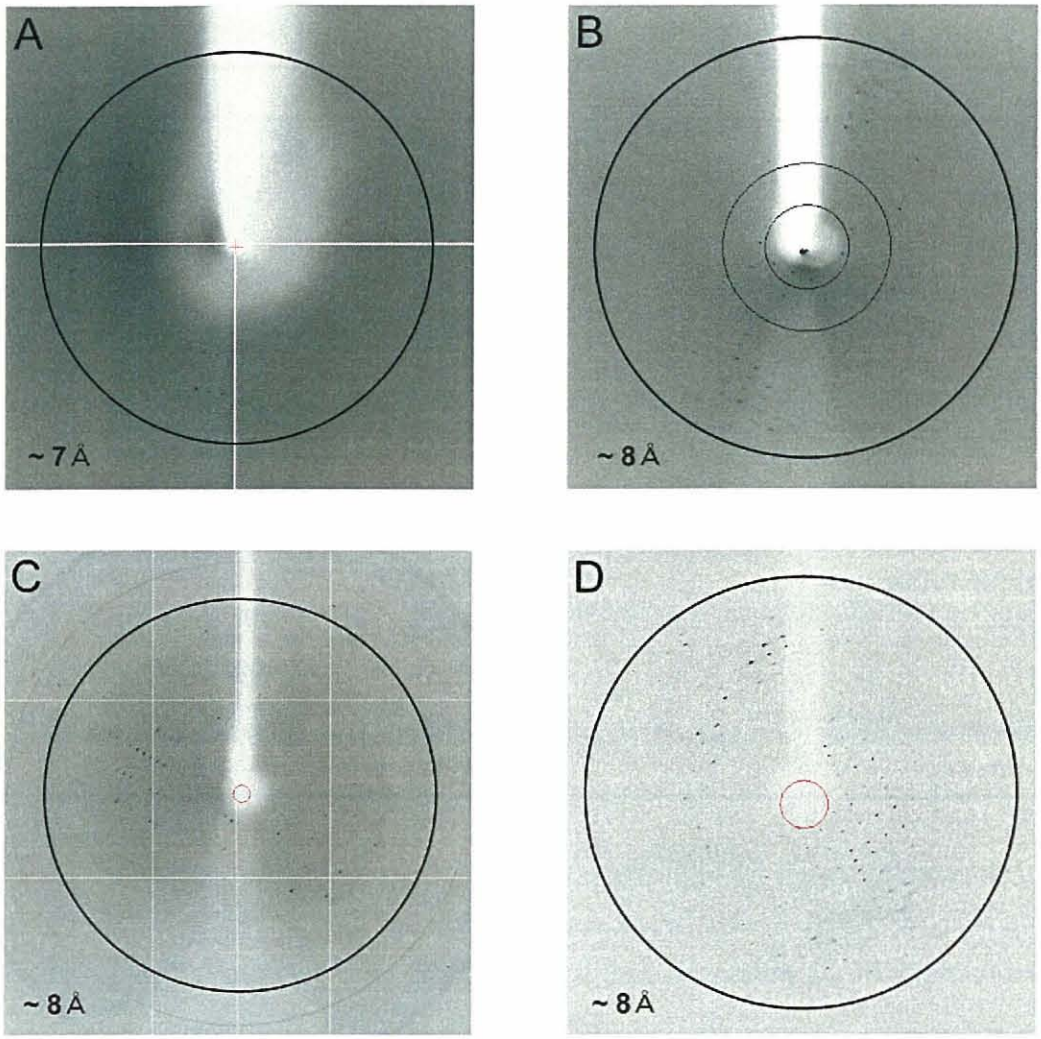

Fig 3. Representative 0.5° oscillation images.

(A) The oscillation image on an optimized rhTDO-ΔN15 crystal using Additive Screen. (B) The oscillation image on a rhTDO-ΔN15 crystal produced by microseeding method. (C) The oscillation image on a rhTDO-ΔN40 crystal. (D) The oscillation image on a rhTDO-ΔN35 crystal.

Table 4. Data-collection statistics for a rhTDO-ΔN35 crystal.

	4PI form
X-ray source	**SPring-8 BL41XU**
Wavelength (Å)	**1.00**
Space group	$P2_1$
Unit-cell parameters	
a / b / c (Å)	**93.1 / 134.3 / 125.9**
α / β / γ (°)	**90 / 91.6 / 90**
Data range (Å)	**50.0-8.00 (8.28-8.00)**
Reflections	
Observations used scaling	**12,443**
Unique reflections	**3,373 (319)**
R_{merge} †	**0.135 (0.426)**
I/σ (I)	**10 (2.5)**
Completeness (%)	**99.8 (99.7)**
Redundancy	**3.7 (3.7)**

Values in parentheses are for highest resolution shell.

† $R_{merge} = \Sigma_{hkl} \Sigma_i |I(hkl)_i - \langle I(hkl) \rangle| / \Sigma_{hkl} \Sigma_i I(hkl)_i$.

REFERENCES

1. Sono, M., Roach, M. P., Coulter, E. D., and Dawson, J. H. (1996) Heme-Containing Oxygenases. *Chem. Rev.* **96**, 2841-2888
2. Mayson, H. S., Fowlks, L., and Peterson, E. (1955) Oxygen transfer and electron transport by the phenolase complex. *J. Am. Chem. Soc.* **77**, 2851-2914
3. Waterman, M. R. (2005) Professor Howard Mason and oxygen activation. *Biochem. Biophys. Res. Commun.* **338**, 7-11
4. Hayaishi, O., Katagiri, M., and Rothberg, S. (1955) Mechanism of the pyrocatechase reaction. *J. Am. Chem. Soc.* **77**, 5450-5451
5. Hayaishi, O., and Nozaki, M. (1969) Nature and mechanisms of oxygenases. *Science* **164**, 389-396
6. Hayaishi, O. (2005) An odyssey with oxygen. *Biochem. Biophys. Res. Commun.* **338**, 2-6
7. Feigelson, P., and Brady, F. O. (1974) *Molecular mechanism of oxygen activation*, Academic Press, New York
8. Higuchi, K., and Hayaishi, O. (1967) Enzymic formation of D-kynurenine from D-tryptophan. *Arch. Biochem. Biophys.* **120**, 397-403
9. Yamamoto, S., and Hayaishi, O. (1967) Tryptophan pyrrolase of rabbit intestine. D- and L-tryptophan-cleaving enzyme or enzymes. *J. Biol. Chem.* **242**, 5260-5266
10. Kotake, Y., and Masayama, T. (1936) Über den mechanismus der kynurenin-bildung aus tryptophan. *Hoppe-Seyler's Z. Physiol. Chem.* **243** 237-244
11. Higuchi, K., Kuno, S., and Hayaishi, O. (1963) Enzymatic formation of D-kynurenine. *Fed. Proc.* **22**, 243
12. Shimizu, T., Nomiyama, S., Hirata, F., and Hayaishi, O. (1978) Indoleamine 2,3-dioxygenase. Purification and some properties. *J. Biol. Chem.* **253**, 4700-4706

13. Hayaishi, O., Rothberg, S., Mehler, A. H., and Saito, Y. (1957) Studies on oxygenases; enzymatic formation of kynurenine from tryptophan. *J. Biol. Chem.* **229**, 889-896

14. Hayaishi, O. (1976) Properties and function of indoleamine 2,3-dioxygenase. *J. Biochem.* **79**, 13-21

15. Muller, A. J., and Prendergast, G. C. (2007) Indoleamine 2,3-dioxygenase in immune suppression and cancer. *Curr. Cancer Drug Targets* **7**, 31-40

16. Takikawa, O. (2005) Biochemical and medical aspects of the indoleamine 2,3-dioxygenase-initiated L-tryptophan metabolism. *Biochem. Biophys. Res. Commun.* **338**, 12-19

17. Mellor, A. L., and Munn, D. H. (2004) IDO expression by dendritic cells: tolerance and tryptophan catabolism. *Nat. Rev. Immunol.* **4**, 762-774

18. Munn, D. H., and Mellor, A. L. (2007) Indoleamine 2,3-dioxygenase and tumor-induced tolerance. *J. Clin. Invest.* **117**, 1147-1154

19. Carlin, J. M., Borden, E. C., Sondel, P. M., and Byrne, G. I. (1987) Biological response modifier-induced indoleamine 2,3-dioxygenase activity in human peripheral blood mononuclear cell cultures. *J. Immunol.* **139**, 2414-2418

20. Yoshida, R., and Hayaishi, O. (1978) Induction of pulmonary indoleamine 2,3-dioxygenase by intraperitoneal injection of bacterial lipopolysaccharide. *Proc. Natl. Acad. Sci. U.S.A.* **75**, 3998-4000

21. Yoshida, R., Urade, Y., Tokuda, M., and Hayaishi, O. (1979) Induction of indoleamine 2,3-dioxygenase in mouse lung during virus infection. *Proc. Natl. Acad. Sci. U.S.A.* **76**, 4084-4086

22. Heyes, M. P., Saito, K., Jacobowitz, D., Markey, S. P., Takikawa, O., and Vickers, J. H. (1992) Poliovirus induces indoleamine-2,3-dioxygenase and quinolinic acid synthesis in macaque brain. *FASEB J.* **6**, 2977-2989

23. Munn, D. H., Zhou, M., Attwood, J. T., Bondarev, I., Conway, S. J., Marshall, B., Brown, C., and Mellor, A. L. (1998) Prevention of allogeneic fetal rejection by tryptophan catabolism. *Science* **281**, 1191-1193

24. Mellor, A. L., Sivakumar, J., Chandler, P., Smith, K., Molina, H., Mao, D., and

Munn, D. H. (2001) Prevention of T cell-driven complement activation and inflammation by tryptophan catabolism during pregnancy. *Nat. Immunol.* **2**, 64-68

25. Fallarino, F., Grohmann, U., Vacca, C., Bianchi, R., Orabona, C., Spreca, A., Fioretti, M. C., and Puccetti, P. (2002) T cell apoptosis by tryptophan catabolism. *Cell Death Differ.* **9**, 1069-1077

26. Taylor, M. W., and Feng, G. S. (1991) Relationship between interferon-gamma, indoleamine 2,3-dioxygenase, and tryptophan catabolism. *FASEB J.* **5**, 2516-2522

27. Muller, A. J., Malachowski, W. P., and Prendergast, G. C. (2005) Indoleamine 2,3-dioxygenase in cancer: targeting pathological immune tolerance with small-molecule inhibitors. *Expert Opin. Ther. Targets* **9**, 831-849

28. Friberg, M., Jennings, R., Alsarraj, M., Dessureault, S., Cantor, A., Extermann, M., Mellor, A. L., Munn, D. H., and Antonia, S. J. (2002) Indoleamine 2,3-dioxygenase contributes to tumor cell evasion of T cell-mediated rejection. *Int. J. Cancer* **101**, 151-155

29. Brastianos, H. C., Vottero, E., Patrick, B. O., Van Soest, R., Matainaho, T., Mauk, A. G., and Andersen, R. J. (2006) Exiguamine A, an indoleamine-2,3-dioxygenase (IDO) inhibitor isolated from the marine sponge Neopetrosia exigua. *J. Am. Chem. Soc.* **128**, 16046-16047

30. Muller, A. J., and Prendergast, G. C. (2005) Marrying immunotherapy with chemotherapy: why say IDO? *Cancer Res.* **65**, 8065-8068

31. Forouhar, F., Anderson, J. L., Mowat, C. G., Vorobiev, S. M., Hussain, A., Abashidze, M., Bruckmann, C., Thackray, S. J., Seetharaman, J., Tucker, T., Xiao, R., Ma, L. C., Zhao, L., Acton, T. B., Montelione, G. T., Chapman, S. K., and Tong, L. (2007) Molecular insights into substrate recognition and catalysis by tryptophan 2,3-dioxygenase. *Proc. Natl. Acad. Sci. U.S.A.* **104**, 473-478

32. Feigelson, P., and Greengard, O. (1962) Regulation of liver tryptophan pyrrolase activity. *J. Biol. Chem.* **237**, 1908-1913

33. Britan, A., Maffre, V., Tone, S., and Drevet, J. R. (2006) Quantitative and spatial

differences in the expression of tryptophan-metabolizing enzymes in mouse epididymis. *Cell. Tissue. Res.* **324**, 301-310

34. Miller, C. L., Llenos, I. C., Dulay, J. R., Barillo, M. M., Yolken, R. H., and Weis, S. (2004) Expression of the kynurenine pathway enzyme tryptophan 2,3-dioxygenase is increased in the frontal cortex of individuals with schizophrenia. *Neurobiol. Dis.* **15**, 618-629
35. Suzuki, S., Tone, S., Takikawa, O., Kubo, T., Kohno, I., and Minatogawa, Y. (2001) Expression of indoleamine 2,3-dioxygenase and tryptophan 2,3-dioxygenase in early concepti. *Biochem. J.* **355**, 425-429
36. Sedlmayr, P., Blaschitz, A., Wintersteiger, R., Semlitsch, M., Hammer, A., MacKenzie, C. R., Walcher, W., Reich, O., Takikawa, O., and Dohr, G. (2002) Localization of indoleamine 2,3-dioxygenase in human female reproductive organs and the placenta. *Mol. Hum. Reprod.* **8**, 385-391
37. Hirata, F., and Hayaishi, O. (1972) New degradative routes of 5-hydroxytryptophan and serotonin by intestinal tryptophan 2,3-dioxygenase. *Biochem. Biophys. Res. Commun.* **47**, 1112-1119
38. Schimke, R. T., Sweeney, E. W., and Berlin, C. M. (1965) The Roles of Synthesis and Degradation in the Control of Rat Liver Tryptophan Pyrrolase. *J. Biol. Chem.* **240**, 322-331
39. Knox, W. E., and Mehler, A. H. (1951) The adaptive increase of the tryptophan peroxidase-oxidase system of liver. *Science* **113**, 237-238
40. Lee, N. D., and Williams, R. H. (1952) Inhibition of adaptive formation of tryptophan peroxidase in rats by ethionine. *Biochim. Biophys. Acta* **9**, 698
41. Knox, W. E., and Auerbach, V. H. (1955) The hormonal control of tryptophan peroxidase in the rat. *J. Biol. Chem.* **214**, 307-313
42. Horton, H. R., and Franz, J. M. (1959) Effect of ethionine on the cortisone-evoked stimulation of tryptophan peroxidase-oxidase activity. *Endocrinology* **64**, 258-261
43. Greengard, O., Smith, M. A., and Acs, G. (1963) Relation of cortisone and synthesis of ribonucleic acid to induced and developmental enzyme formation. *J.*

Biol. Chem. **238**, 1548-1551

44. Schutz, G., Killewich, L., Chen, G., and Feigelson, P. (1975) Control of the mRNA for hepatic tryptophan oxygenase during hormonal and substrate induction. *Proc. Natl. Acad. Sci. U.S.A.* **72**, 1017-1020

45. Wagner, C., and Brown, A. T. (1970) Regulation of tryptophan pyrrolase activity in Xanthomonas pruni. *J. Bacteriol.* **104**, 90-97

46. Cho-Chung, Y. S., and Pitot, H. C. (1967) Feedback control of rat liver tryptophan pyrrolase. I. End product inhibition of trytophan pyrrolase activity. *J. Biol. Chem.* **242**, 1192-1198

47. Schutz, G., Chow, E., and Feigelson, P. (1972) Regulatory properties of hepatic tryptophan oxygenase. *J. Biol. Chem.* **247**, 5333-5337

48. Sugimoto, H., Oda, S., Otsuki, T., Hino, T., Yoshida, T., and Shiro, Y. (2006) Crystal structure of human indoleamine 2,3-dioxygenase: catalytic mechanism of O2 incorporation by a heme-containing dioxygenase. *Proc. Natl. Acad. Sci. U.S.A.* **103**, 2611-2616

49. Zhang, Y., Kang, S. A., Mukherjee, T., Bale, S., Crane, B. R., Begley, T. P., and Ealick, S. E. (2007) Crystal structure and mechanism of tryptophan 2,3-dioxygenase, a heme enzyme involved in tryptophan catabolism and in quinolinate biosynthesis. *Biochemistry* **46**, 145-155

50. Koike, K., and Feigelson, P. (1971) Studies on the catalytic and allosteric sites in modulating the reactivity of tryptophan oxygenase with heme ligands. II. Carbon monoxide derivatives. *Biochemistry* **10**, 3385-3390

51. Koike, K., and Feigelson, P. (1971) Studies on the roles of the catalytic and allosteric sites in modulating the reactivity of tryptophan oxygenase with heme ligands. I. Cyanide derivatives. *Biochemistry* **10**, 3378-3384

52. Ishimura, Y., Nozaki, M., and Hayaishi, O. (1967) Evidence for an oxygenated intermediate in the tryptophan pyrrolase reaction. *J. Biol. Chem.* **242**, 2574-2576

53. Maeno, H., and Feigelson, P. (1968) Tryptophan and alpha-methyltryptophan facilitation in the interaction of cyanide with tryptophan oxygenase. *Biochemistry* **7**, 968-970

54. Yoshida, T., Lorence, R. M., Choc, M. G., Tarr, G. E., Findling, K. L., and Fee, J. A. (1984) Respiratory proteins from the extremely thermophilic aerobic bacterium, Thermus thermophilus. Purification procedures for cytochromes c552, c555,549, and c1aa3 and chemical evidence for a single subunit cytochrome aa3. *J. Biol. Chem.* **259**, 112-123

55. Paul, K. G., Theorell, H., and Akeson, A. (1953) The molar light absorption of pyridine ferroprotoporphyrin (pyridine hemochromogen). *Acta. Chem. Scand.* **7**, 1284-1287

56. Falk, J. E. (1964) Absorption spectra in *B.B.A. Library 2, Porphyrins and metalloporphyrins*, pp. 231-246, Elsevier Publishing, Amsterdam.

57. Ishimura, Y., Nozaki, M., and Hayaishi, O. (1970) The oxygenated form of L-tryptophan 2,3-dioxygenase as reaction intermediate. *J. Biol. Chem.* **245**, 3593-3602

58. Thackray, S. J., Bruckmann, C., Anderson, J. L., Campbell, L. P., Xiao, R., Zhao, L., Mowat, C. G., Forouhar, F., Tong, L., and Chapman, S. K. (2008) Histidine 55 of tryptophan 2,3-dioxygenase is not an active site base but regulates catalysis by controlling substrate binding. *Biochemistry* **47**, 10677-10684

59. DeLano, W. L. (2002) *The PyMOL Molecular Graphics System*, DeLano Scientific, San Carlos, CA, USA.

60. Gouet, P., Courcelle, E., Stuart, D. I., and Metoz, F. (1999) ESPript: analysis of multiple sequence alignments in PostScript. *Bioinformatics* **15**, 305-308

61. Thompson, J. D., Higgins, D. G., and Gibson, T. J. (1994) CLUSTAL W: improving the sensitivity of progressive multiple sequence alignment through sequence weighting, position-specific gap penalties and weight matrix choice. *Nucleic. Acids. Res.* **22**, 4673-4680

62. Batabyal, D., and Yeh, S. R. (2007) Human tryptophan dioxygenase: a comparison to indoleamine 2,3-dioxygenase. *J. Am. Chem. Soc.* **129**, 15690-15701

63. Martin-Nieto, J., Flores, E., and Herrero, A. (1992) Biphasic Kinetic Behavior of Nitrate Reductase from Heterocystous, Nitrogen-Fixing Cyanobacteria. *Plant*

Physiol. **100**, 157-163

64. Pant, K. C., Rogers, Q. R., and Harper, A. E. (1974) Plasma and tissue free amino acid concentrations in rats fed tryptophan-imbalanced diets with or without niacin. *J. Nutr.* **104**, 1584-1596

65. Varadarajan, R., Lambright, D. G., and Boxer, S. G. (1989) Electrostatic interactions in wild-type and mutant recombinant human myoglobins. *Biochemistry* **28**, 3771-3781

66. Hu, S., Smith, K. M. & Spiro, T. G. (1996) Assignment of Protoheme Resonance Raman Spectrum by Heme Labeling in Myoglobin *J. Am. Chem. Soc.* **118**, 12638 -12646

67. Rousseau, D. L., Ching, Y. C., Brunori, M., and Giacometti, G. M. (1989) Axial coordination of ferric Aplysia myoglobin. *J. Biol. Chem.* **264**, 7878-7881

68. Chen, Z., Ost, T. W., and Schelvis, J. P. (2004) Phe393 mutants of cytochrome P450 BM3 with modified heme redox potentials have altered heme vinyl and propionate conformations. *Biochemistry* **43**, 1798-1808

69. Michael, A. F., Drummond, K. N., Doeden, D., Anderson, J. A., and Good, R. A. (1964) Tryptophan Metabolism in Man. *J. Clin. Invest.* **43**, 1730-1746

70. Stone, T. W. (1993) Neuropharmacology of quinolinic and kynurenic acids. *Pharmacol. Rev.* **45**, 309-379

71. Nutt, D. J. (2008) Relationship of neurotransmitters to the symptoms of major depressive disorder. *J. Clin. Psychiatry* **69 Suppl E1**, 4-7

72. Ener, R. A., Meglathery, S. B., Van Decker, W. A., and Gallagher, R. M. (2003) Serotonin syndrome and other serotonergic disorders. *Pain Med.* **4**, 63-74

73. Dick, R., Murray, B. P., Reid, M. J., and Correia, M. A. (2001) Structure--function relationships of rat hepatic tryptophan 2,3-dioxygenase: identification of the putative heme-ligating histidine residues. *Arch. Biochem. Biophys.* **392**, 71-78

74. Basran, J., Rafice, S. A., Chauhan, N., Efimov, I., Cheesman, M. R., Ghamsari, L., and Raven, E. L. (2008) A kinetic, spectroscopic, and redox study of human tryptophan 2,3-dioxygenase. *Biochemistry* **47**, 4752-4760

75. Blodig, W., Doyle, W. A., Smith, A. T., Winterhalter, K., Choinowski, T., and Piontek, K. (1998) Autocatalytic formation of a hydroxy group at C beta of trp171 in lignin peroxidase. *Biochemistry* **37**, 8832-8838

76. Pogni, R., Baratto, M. C., Teutloff, C., Giansanti, S., Ruiz-Duenas, F. J., Choinowski, T., Piontek, K., Martinez, A. T., Lendzian, F., and Basosi, R. (2006) A tryptophan neutral radical in the oxidized state of versatile peroxidase from Pleurotus eryngii: a combined multifrequency EPR and density functional theory study. *J. Biol. Chem.* **281**, 9517-9526

77. Yagil, G. (1967) The proton dissociation constant of pyrrole, indole and related compounds. *Tetrahedron* **23**, 2855-2861

78. Center, R. J., Kobe, B., Wilson, K. A., Teh, T., Howlett, G. J., Kemp, B. E., and Poumbourios, P. (1998) Crystallization of a trimeric human T cell leukemia virus type 1 gp21 ectodomain fragment as a chimera with maltose-binding protein. *Protein Sci.* **7**, 1612-1619

79. McPherson, A. (1982) *Preparation and Analysis of Protein Crystals*, Wiley, New York

80. Luft, J. R., and DeTitta, G. T. (1999) A method to produce microseed stock for use in the crystallization of biological macromolecules. *Acta Crystallogr. D Biol. Crystallogr.* **55**, 988-993

81. Chayen, N. E. (1997) The role of oil in macromolecular crystallization. *Structure* **5**, 1269-1274

82. Otwinowski, Z., and Minor, W. (1997) Processing of X-ray diffraction data collected in oscillation mode. *Meth. Enzymol.* **276**, 307-326

ACKNOWLEDGEMENTS

I would like to express great appreciation to Professor Y. Shiro and Dr. H. Sugimoto for their continuing guidance and many valuable discussions. I am much indebted to Dr. K. Takio and Ms. N. Takahashi for their help with the N-terminal amino acid sequence analysis. I am grateful to Professor T. Ogura (University of Hyogo) and Ms. Y. Misumi for their help with the resonance Raman spectroscopic measurements and insightful comments and suggestions. I also thank Research Infrastructure Group (RIKEN SPring-8 center) and Japan Synchrotron Radiation Research Institute (JASRI) for the operation of the SPring-8 synchrotron beam lines, BL44B2 and BL41XU. I thank my colleagues in Biometal Science Laboratory (Professor Shiro's laboratory) for not only their kind help in this study but also their encouragement and supports over the years. Finally, I render thanks to my friends and my family who gave me a lot of encouragement.

LIST OF PUBLICATIONS

1. Fukumura, E., Sugimoto, H., Misumi, Y., Ogura, T. and Shiro, Y. (2009)
   Cooperative Biding of L-Trp to Human Tryptophan 2,3-Dioxygenase: Resonance Raman Spectroscopic Analysis. *J.Biochem., in press*.

2. Kikuchi, A., Fukumura, E., Karasawa, S., Mizuno, H., Miyawaki, A. and Shiro, Y. (2008)
   Structural Characterization of a Thiazoline-Containing Chromophore in an Orange Fluorescent Protein, Monomeric Kusabira Orange. *Biochemistry*, **47**, 11573-11580

3. Kikuchi, A., Fukumura, E., Karasawa, S., Shiro, Y. and Miyawaki, A. (2009)
   Crystal Structure of a New Cyan Fluorescent Protein and its Hue-Shifted Variants. *Biochiemistry, in press.*